Article

Gene transcription, neurotransmitter, and neurocognition signatures of brain structural-functional coupling variability

Lin Jiang [1,2,3], Sarah Genon [4,5], Jiayu Ye[1,2], Yan Zhu[1,2], Guangying Wang[1,2], Runyang He[1,2], Pedro A. Valdes-Sosa[1,2,6], Feng Wan[7], Dezhong Yao [1,2,8,9] ✉, Simon B. Eickhoff [4,5], Debo Dong [4,10] ✉, Fali Li [1,2,9] ✉ & Peng Xu [1,2,9] ✉

The relationship between brain structure and function, known as structural-functional coupling (SFC), is highly dynamic. However, the temporal variability of this relationship, referring to the fluctuating extent to which functional profiles interact with anatomy over time, remains poorly elucidated. Here, we propose a framework to quantify SFC temporal variability and determine its neurocognitive map, genetic architecture, and neurochemical basis in 1206 healthy human participants. Results reveal regional heterogeneity in SFC variability and a composite emotion dimension co-varying with variability patterns involving the dorsal attention, somatomotor, and visual networks. The transcriptomic signatures of SFC variability are enriched in synapse- and cell cycle-related biological processes and implicated in emotion-related disorders. Moreover, regional densities of serotonin, glutamate, γ-aminobutyric acid, and opioid systems are predictive of SFC variability across the cortex. Collectively, SFC variability mapping provides a biologically plausible framework for understanding how SFC fluctuates over time to support macroscale neurocognitive specialization.

The central objective of network neuroscience is to understand how dynamic neural communication propagates through complex anatomy and ultimately contributes to the diverse repertoire of the brain[1,2]. This has naturally propelled brain research towards investigating the intricate relationship between structural and functional neural connections, leading to the emergence of structure-function coupling (SFC), which aims to reveal the statistical dependence of a brain area's function on its underlying structure[3].

Historically, most studies have calculated SFC as a static variable, further examining its relationships with age[4], heritability[5], and disease[6]. However, the human brain is an inherently dynamic system. In contrast to the anatomically grounded and relatively stable brain structure, functional connectivity fluctuates across multiple temporal and spatial scales, giving rise to the rich dynamics of brain SFC[7,8]. To this end, it is reasonable to hypothesize that, rather than a static quantity, the SFC should fluctuate over multiple timescales to support

[1]The Clinical Hospital of Chengdu Brain Science Institute, MOE Key Lab for Neuroinformation, School of Life Science and Technology, University of Electronic Science and Technology of China, Chengdu 611731, China. [2]Brain-Computer Interface & Brain-Inspired Intelligence Key Laboratory of Sichuan Province, University of Electronic Science and Technology of China, Chengdu 611731, China. [3]Key Laboratory of Computational Neuroscience and Brain-Inspired Intelligence, Fudan University, Shanghai 200433, China. [4]Institute of Neuroscience and Medicine, Brain and Behavior (INM-7), Research Center Jülich, Jülich, Germany. [5]Institute for Systems Neuroscience, Medical Faculty, Heinrich-Heine University Düsseldorf, Düsseldorf, Germany. [6]Cuban Center for Neurocience, La Habana, Cuba. [7]Department of Electrical and Computer Engineering, Faculty of Science and Technology, University of Macau, Macau, China. [8]School of Electrical Engineering, Zhengzhou University, Zhengzhou 450001, China. [9]Research Unit of NeuroInformation, Chinese Academy of Medical Sciences, 2019RU035 Chengdu, China. [10]Faculty of Psychology, Southwest University, Chongqing 400715, China. ✉e-mail: dyao@uestc.edu.cn; debo.dong@gmail.com; fali.li@uestc.edu.cn; xupeng@uestc.edu.cn

flexible reconfiguration and switching among multitudinous brain systems. Theoretically, the greater diversity in fluctuating patterns of a given SFC time course, the higher temporal variability exhibited by the corresponding time course, thereby indexing its fluctuating dynamics. Whereas no previous study has quantified the temporal variability of dynamic SFC, reflecting the fluctuating extent to which functional connections interact with anatomical structures over time. Given that structure constrains brain functional dynamics during cognitive processes, estimating the temporal variability of cortical dynamic SFC may be an alternative and more integrated indicator of the individual brain functional phenotype, and could therefore potentially be used to better understand brain-behavior relationships and neurocognitive alterations in clinical populations.

Hence, in the current work, a computational framework was developed to quantify the temporal variability of cortical dynamic SFC using multimodal magnetic resonance imaging (MRI). Firstly, by calculating the element-wise product of all pairs of functional MRI (fMRI) signals, the edge time series were generated to depict the inter-regional co-fluctuation magnitude of instantaneous functional activity[9]. Meanwhile, the morphometric similarity network (MSN)[10], which serves as a proxy for the brain's axonal connectivity, was employed to examine inter-regional structural organization. Then, the morphometric similarity connectivity of each region was correlated with the corresponding region's edge time series at each time point, yielding the regional dynamic series of SFC. Finally, fuzzy entropy[11] was utilized to quantify the temporal variability of the time-varying SFC series. Of note, in comparison with traditional measures, such as variance, fuzzy entropy has been proven to be a more accurate measure of variability, as it is insensitive to data magnitude and instead relies more on data distribution[11]. Moreover, fuzzy entropy not only exhibits stronger relative consistency and less dependence on data length, implying less bias, but also achieves continuity, freer parameter selections, and more robustness to noise[12]. Thus, fuzzy entropy is potentially more helpful in capturing the inherent dynamic fluctuation patterns of SFC. Notably, SFC temporal variability integrates high spatial resolution details of both structure and function, further enriched by fine-grained temporal dynamics, facilitating a more precise and lightweight delineation of the high-dimensional spatiotemporal characteristics of human cognition.

Essentially, the remarkable complexity of the human brain arises from its precise circuitry, structural and cellular diversity, and ultimately from the regulation of its underlying transcriptome[13]. Nevertheless, MRI-based macroscopic imaging exhibits limited specificity for capturing the molecular and cellular characteristics of brain tissues[14,15]. This has limited the capacity of temporal variability metrics to elucidate the biological processes driving brain cognition and to inform mechanistic models of brain diseases. The availability of brain-wide gene expression atlases (e.g., Allen Human Brain Atlas (AHBA)[13]) and the advancement of curated processing pipelines[16,17], enable the reliable identification of transcriptional patterns associated with macroscale anatomical and functional brain organization[16,18]. Rather than reflecting inherited genetic variation, these data capture cell-type-specific and spatially patterned gene expression profiles, offering a molecular lens for interpreting macroscale neuroimaging phenotypes. In addition, chemoarchitecture, i.e., the neurotransmitter transporter and receptor, represents another important molecular annotation for clarifying the intricate relationship between brain structure and function[19,20]. Elucidating the corresponding transcriptional and chemoarchitectural landscape could be crucial for decoding the molecular mechanism underlying brain SFC temporal variability. Whereas, to our current understanding, no previous study to date has characterized the temporal variability of cortical dynamic SFC; hence, the underlying molecular mechanisms are, thus far, unknown.

In this work, we explore how macroscopic structure and function are intertwined over time to affect human cognition or be modulated by brain-wide gene expression and neurotransmitter receptors. Specifically, leveraging time- and region-resolved SFC patterns, we propose a framework to estimate the temporal variability of cortical dynamic SFC. Results reveal that SFC temporal variability is spatially organized, with higher variability spanning the anterior and posterior cortex, while stable SFC is observed in the intermediate cortex, reflecting the existence of distinct cortical hierarchies. Additionally, SFC temporal variability distributed in the dorsal attention, somatomotor, and visual networks is closely linked to a composite emotion dimension. More interestingly, the transcriptomic organizations of cortical SFC variability are enriched in synapse- and cell cycle-related biological processes, associated with excitatory neurons, and consistently implicated in disorders pertaining to emotion. Finally, we unveil an integrated spatial topography of serotonin, glutamate, γ-aminobutyric acid, and opioid systems that manifest as regionally specialized SFC variability across the cortex. Together, cortical SFC variability delineates a critical neuroimaging-derived dimension of human brain operation, wherein divergent neurotransmitomic, transcriptomic, and cellular signatures are expressed to support SFC fluctuations over time, thereby regulating cognition specialization.

Results
Study overview
Herein, leveraging multimodal neuroimaging data and behavioral measures of 1206 participants from the Human Connectome Project (HCP, S1200 release)[21] and 366 participants from the Chinese HCP (CHCP)[22], we first quantified the replicable temporal variability pattern of cortical dynamic SFC (Fig. 1a). Specifically, we extracted the resting-state fMRI signals per region of interest (ROI) utilizing the Desikan-Killiany (D-K) atlas[23] (308 ROIs). The temporal unwrapping procedure was then performed to generate moment-to-moment functional co-fluctuation matrices with the dimensionality of $308 \times 308 \times time$. These matrices represent the instantaneous functional co-fluctuation magnitudes between pairwise ROIs in the form of edge time series (Step 1 of Fig. 1a). Meanwhile, as displayed in Step 2 of Fig. 1a, the MSN with the dimensionality of 308×308 was constructed based on multimodal morphological features derived from structural MRI (sMRI) and diffusion MRI (dMRI). Then, each column in the morphometric similarity matrix was correlated (via Pearson's correlation) with the same region's column in the edge time series profile at each time point, generating the regional time-varying SFC series with the dimensionality of $308 \times time$ per participant. Fuzzy entropy[11] was applied to quantify the fluctuating dynamics of SFC over time, whereby defined as the temporal variability of SFC (or referred to as SFC variability; Step 3 of Fig. 1a).

Thereafter, the multivariate relationship between SFC temporal variability and multiple cognitive and behavioral traits was investigated by partial least squares analysis (PLS; Fig. 1b). By integrating transcriptomics data from AHBA[13] and positron emission tomography (PET) images collected from 1200+ healthy individuals[19], we further explore the underlying relationships between SFC variability and brain-wide gene expression (Fig. 1c), along with neurochemical architecture (Fig. 1d). Herein, the CHCP cohort was used to validate the reproducibility of cortical SFC temporal variability and the corresponding transcriptome-neuroimaging association.

Hierarchical organization of cortical SFC variability
The grand-averaged cortical SFC variability over all participants is shown in Fig. 2a. We then applied a threshold strategy to refine the cortical distribution of SFC variability to specific hierarchical brain regions. Concretely, the 10% to 50% cortical regions with the largest (Fig. 2b) and smallest fuzzy entropy (Fig. 2c) were extracted to index the complementary spatial architectures of SFC variability. Of note, the temporal fluctuation of regional SFC exhibited significant
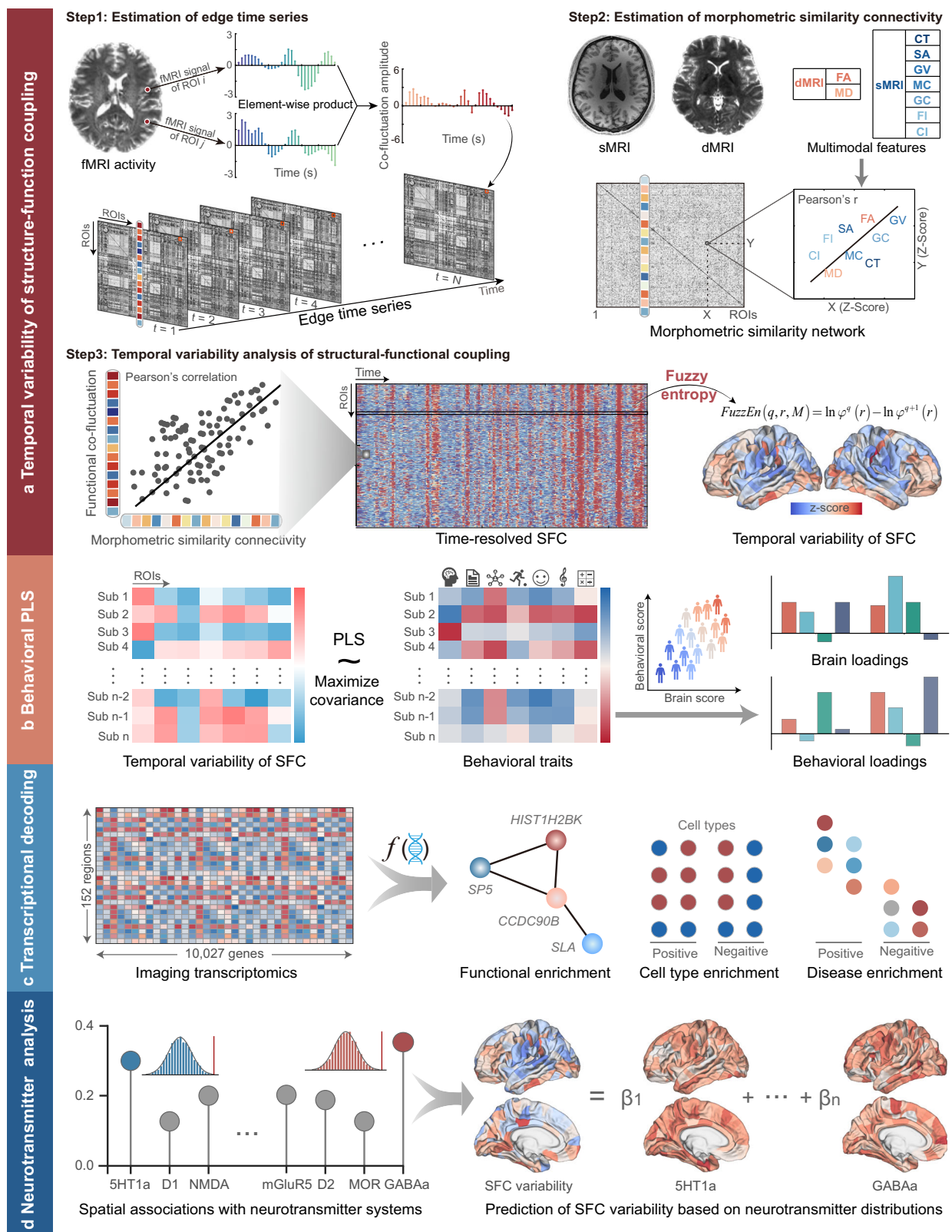
variations across brain regions, with greater variability observed in the prefrontal and occipital cortex (Fig. 2b), while lower variability was found in frontal and parietal regions (Fig. 2c). Next, to enhance the generalizability of our findings across different levels of brain organization, we also allocated ROIs from the D–K atlas to Yeo 7 functional networks[24] and the von Economo cytoarchitectonic classes[25]. In Fig. 2d, participants showed relatively large cortical SFC variability in the Yeo limbic network (LN) and visual network (VN), while that of the somatomotor network (SMN), dorsal attention network (DAN), and ventral attention network (VAN) was relatively small. Interestingly, for the von Economo cytoarchitectonic classes, we found consistently higher cortical SFC variability in secondary sensory and limbic cytoarchitectonic classes in Fig. 2e.

Fig. 1 | Study overview. a Estimating temporal variability of structure-function coupling (SFC). Step 1: Estimation of edge time series with the dimensionality of 308 × 308 × time via computing the element-wise product of pairwise Z-scored fMRI signals. Step 2: Estimation of morphometric similarity connectivity with the dimensionality of 308 × 308 based on nine sMRI and dMRI features. Step 3: The regional time-resolved SFC series, with the dimensionality of 308 × time, is computed by correlating a region's morphometric similarity and functional co-fluctuation profile at each time point; subsequently, the temporal variability of dynamic SFC is quantified by fuzzy entropy. **b** Behavioral partial least squares (PLS) analysis. PLS is adopted to delineate multivariate relationships between SFC variability and 59 behavioral measures spanning multiple domains of cognition, emotion, motor, sensory, alertness, and personality. **c** Transcriptional decoding of SFC temporal variability. Imaging-transcriptomic associations are revealed by PLS, and enrichment analyses are conducted using PLS1 genes. **d** Neurotransmitter analysis of SFC temporal variability. Spatial correlations between SFC variability and neurotransmitter densities are examined, and a multiple linear regression model is fitted to predict SFC variability from receptor distributions.
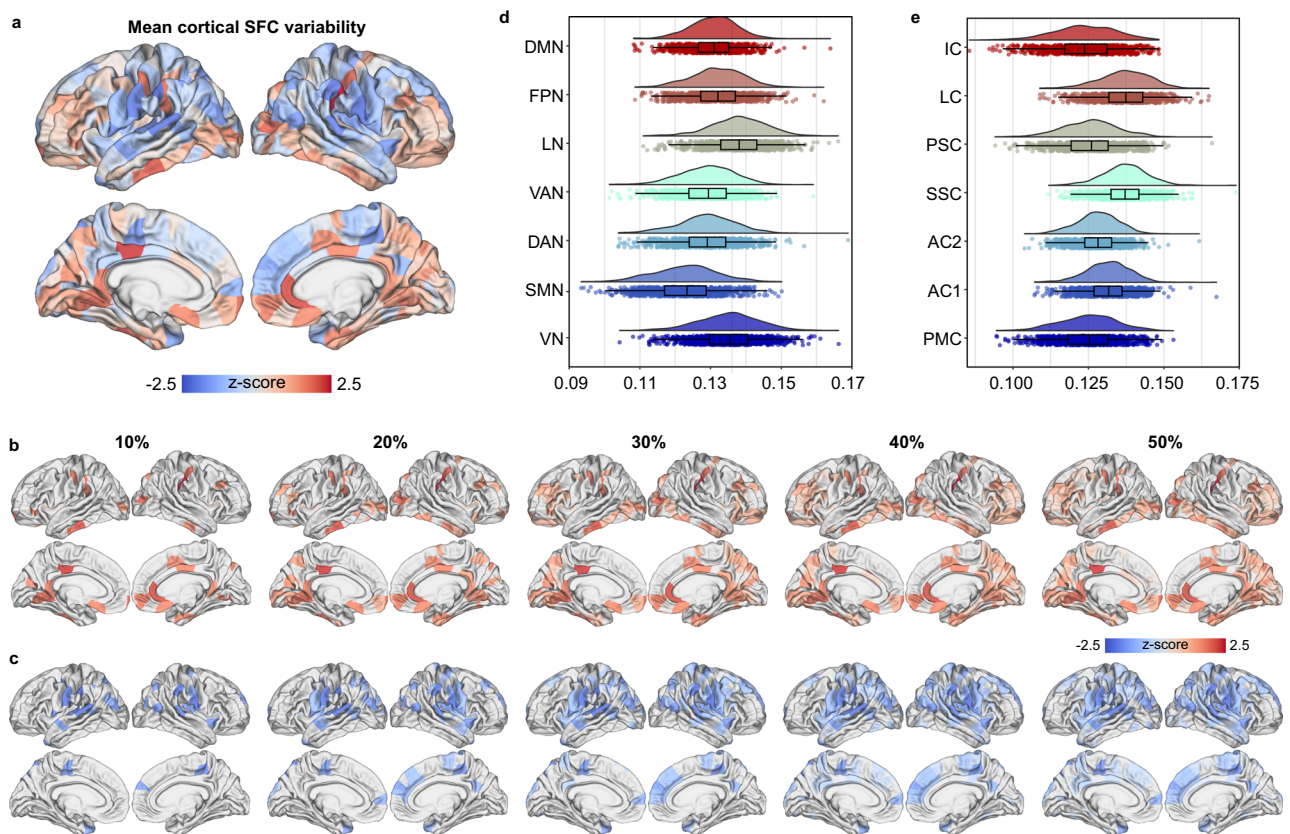
Fig. 2 | Hierarchical cortical SFC variability distribution. a Topographic distribution of brain SFC variability based on the D–K atlas. **b** Hierarchical distributions of brain SFC variability with the 10% to 50% largest fuzzy entropy. **c** Hierarchical distributions with the 10% to 50% smallest fuzzy entropy. **d** The distribution of SFC variability over regions grouped into YEO 7 functional subnetworks. VAN-ventral attention network, LN-limbic network, DAN-dorsal attention network, FPN-frontoparietal network, SMN-somatomotor network, DMN-default mode network, VN-visual network. **e** The distribution of SFC variability over regions grouped into 7 von Economo cytoarchitectonic classes. PMC-primary motor class, AC1-association class 1, AC2-association class 2, SSC-secondary sensory class, PSC-primary sensory class, LC-limbic class, IC-insula class. Boxplots represent the median and upper/lower quartile with whiskers extending to the most extreme data point within 1.5 interquartile ranges above/below the quartiles. Dots show data from $n = 991$ participants. Source data are provided as a Source Data file.

SFC variability complies with structural and functional organization

Theoretically, SFC temporal variability can be regarded as the dynamic perturbations of functional neural activities to the intrinsic structural framework over time. We thereby investigate to what extent the SFC variability complies with the corresponding structural connectivity, functional connectivity, and traditional static SFC configuration. First, the MSN was constructed based on Fig. 1b, while the functional network was obtained using Pearson's correlation of pairwise fMRI signals. To keep consistent with the spatial dimension of cortical SFC variability, the degree of MSN and the functional network was calculated and Z-scored separately to exhibit the regional structural connectivity (Fig. 3a) and functional connectivity (Fig. 3b). In addition, the traditional static SFC was computed by correlating the morphometric similarity connectivity and functional connectivity profiles of each region, followed by Z-scoring (Fig. 3c).

Next, we performed spatial correlations to investigate the potential associations between SFC temporal variability (Fig. 3d) and other brain connectome measures, as exhibited in Fig. 3e. Firstly, consistent with previous findings[3], regional structural connectivity exhibits a significantly positive correlation with functional connectivity ($r_{(306)} = 0.65$, $p_{spin} < 0.001$; a "*spin*"-based method[26] was adopted to correct the spatial autocorrelation), supporting the hypothesis that structural connectome serves as the foundation for the emergence of functional communications[27]. Intuitively, the estimation of SFC is directly dependent on morphometric similarity and functional connectivity, suggesting a close relationship between SFC and these two variables. However, a significant positive association was only found between SFC and structural connectivity ($r_{(306)} = 0.73$, $p_{spin} < 0.001$), while a weak but statistically non-significant positive correlation was found between SFC and functional connectivity ($r_{(306)} = 0.25$, $p_{spin} = 0.22$). Of note, results in Fig. 3e further reveal that
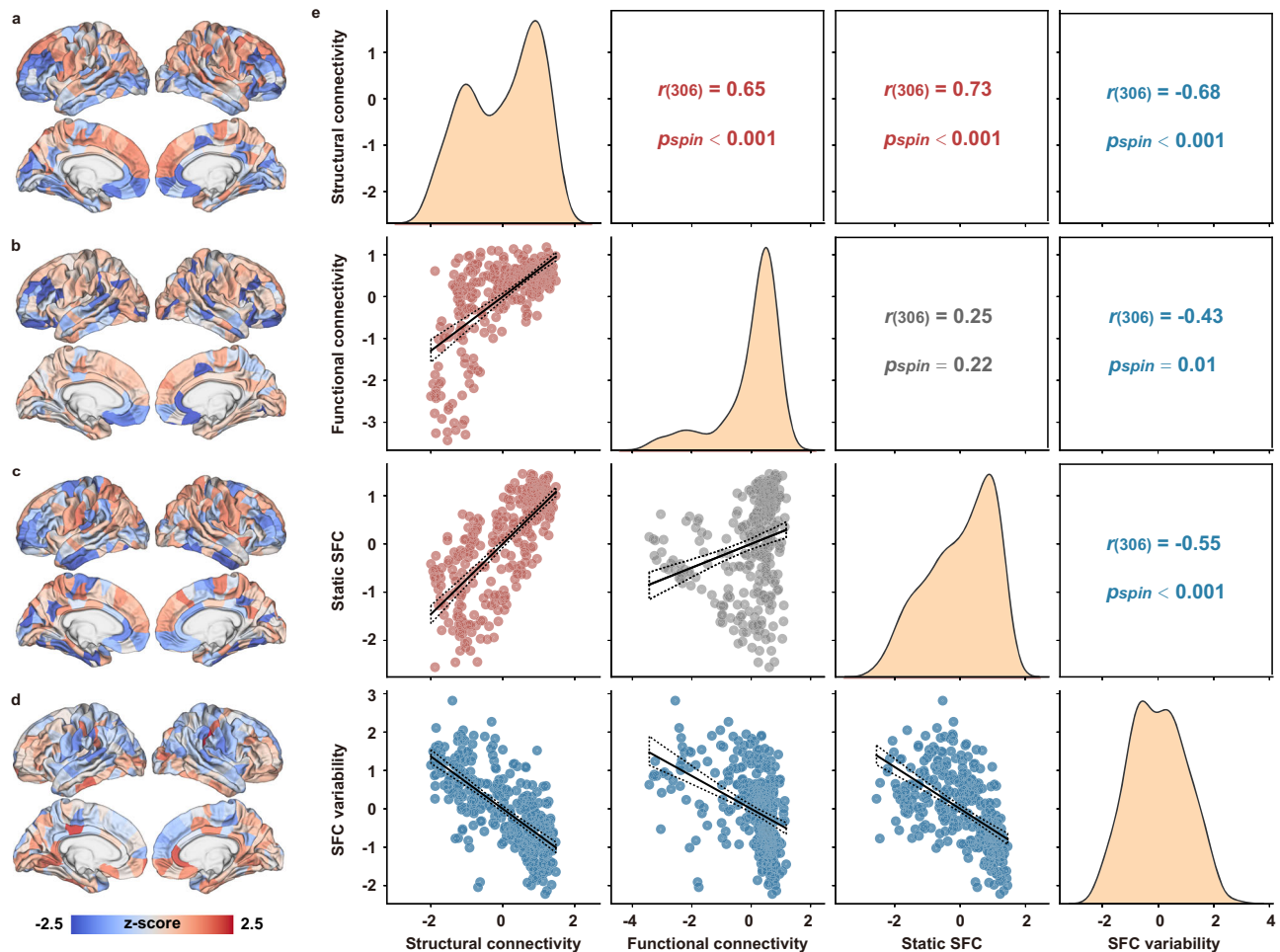
Fig. 3 | Spatial correlation of multiple brain connectome measures. Cortical distribution of brain **a** structural connectivity, **b** functional connectivity, **c** static SFC, and **d** SFC temporal variability for each cortical region in the D-K atlas. **e** Scatter matrix (below the main diagonal) and Pearson's correlation coefficients (above the main diagonal) indicate the interrelationships between structural connectivity, functional connectivity, static SFC, and SFC variability. Red (blue) colored scatter plot indicates a statistically significant positive (negative) correlation between two variables ($p_{spin} < 0.05$), while that in gray suggests no significant correlation ($p_{spin} > 0.05$). All p-values were derived from spin tests and were determined based on one-sided tests. Diagonal density plots indicate the distribution of each connectome measure. Source data are provided as a Source Data file.

SFC variability was significantly negatively related to structural connectivity ($r_{(306)} = -0.68$, $p_{spin} < 0.001$), functional connectivity ($r_{(306)} = -0.43$, $p_{spin} = 0.01$), and even the SFC ($r_{(306)} = -0.55$, $p_{spin} < 0.001$x). These observations indicate that SFC variability effectively integrates the complex spatiotemporal characteristics of the cerebral cortex, thereby providing a more comprehensive representation of brain structure and dynamic function compared to conventional static SFC. Additionally, analysis of the relationship between SFC temporal variability and fMRI autocorrelation revealed a significant negative correlation ($r_{(306)} = -0.69$, $p_{spin} = 1.93 \times 10^{-44}$; Supplementary Results 1 and Fig. S1), suggesting that SFC temporal variability may reflect underlying fMRI autocorrelation.

SFC variability represents a composite dimension of emotion domain

Referred to as the cornerstone of cognitive processes and a diverse repertoire of behaviors, there is an escalating acknowledgment of the interconnections between distributed brain regions in terms of their structural organization and functional dynamics[3,4]. Herein, PLS was thereby applied to examine the multivariate relationships between SFC variability and 59 available behavioral measures (Table 1) in the HCP cohort. The quantity of covariance accounted for by each latent component is illustrated in Fig. 4a. Of note, after conducting

permutation testing with FDR correction, only the first latent component remained statistically significant ($p_{FDR} = 5.60 \times 10^{-3}$), which explained 19.42% of SFC variability-behavior covariance (Fig. 4a). Meanwhile, SFC temporal variability and behavioral composite scores (Fig. 4b) shown a significant positive correlation ($r_{(989)} = 0.14$, $p = 1.61 \times 10^{-5}$). To further validate the robustness of the first latent component, instead of regressing out age and sex, these variables were incorporated into the behavioral data for PLS analysis. The results remained largely consistent, as evidenced by the high correlations between the salience (SFC variability salience: $r = 0.99$, $p = 2.89 \times 10^{-74}$; behavioral salience: $r = 0.99$, $p = 8.39 \times 10^{-242}$; Supplementary Fig. S2) of the original PLS and PLS with age and sex added into the behavioral data.

Thereafter, to assess the contribution of a given SFC variability or behavior to the first latent component, Pearson's correlations between the original SFC variability (or behavioral measure) and the corresponding composite scores were computed[28]. A large correlation value (i.e., large weight, positive or negative) for a given SFC variability or behavioral measure indicates a greater contribution of the SFC variability (or behavior) to the first latent component. Figure 4c illustrates the associations between the behavioral composite score of the first latent component and 30 significant behavioral traits at the group level. The detailed Pearson's correlation coefficients of all 59

Table 1 | Behavioral measures of the HCP cohort (*n* = 991)

Domain	Subdomain	Measure Name	CC	SD	p
Alertness	Cognitive Status	Mini-Mental Status Exam Total Score	−0.10	0.05	0.03
	Sleep	Pittsburgh Sleep Quality Index Total Score	0.45	0.05	<0.001*
	Subjective sleep quality	Pittsburgh Sleep Quality Index Component 1 Score	0.34	0.04	<0.001*
	Sleep latency	Pittsburgh Sleep Quality Index Component 2 Score	0.35	0.04	<0.001*
	Sleep duration	Pittsburgh Sleep Quality Index Component 3 Score	0.15	0.05	<0.001*
	Habitual sleep efficiency	Pittsburgh Sleep Quality Index Component 4 Score	0.17	0.05	<0.001*
	Sleep disturbances	Pittsburgh Sleep Quality Index Component 5 Score	0.22	0.04	<0.001*
	Use of sleep medications	Pittsburgh Sleep Quality Index Component 6 Score	0.15	0.04	<0.001*
	Daytime dysfunction	Pittsburgh Sleep Quality Index Component 7 Score	0.43	0.04	<0.001*
Cognition	Episodic memory	Picture Sequence Memory Test	0.03	0.05	0.62
	Executive function/Cognitive flexibility	Dimensional Change Card Sort Test	0.03	0.06	0.61
	Executive function/inhibition	Flanker Inhibitory Control and Attention Test	0.04	0.05	0.45
	Fluid intelligence	Penn Progressive Matrices	0.03	0.06	0.62
	Language/reading decoding	Oral Reading Recognition Test	0.03	0.07	0.62
	Language/vocabulary comprehension	Picture Vocabulary Test	−0.02	0.06	0.72
	Processing speed	Pattern Comparison Processing Speed Test	−0.01	0.05	0.77
	Self-regulation/ impulsivity	Delay Discounting: Area Under the Curve for Discounting of $200	−0.03	0.05	0.51
	Self-regulation/ impulsivity	Delay Discounting: Area Under the Curve for Discounting of $40,000	−0.01	0.05	0.82
	Spatial orientation	Variable Short Penn Line Orientation Test	0.02	0.06	0.76
	Sustained attention	Short Penn Continuous Performance Test_Sensitivity	0.01	0.05	0.77
	Sustained attention	Short Penn Continuous Performance Test_Specificity	−0.05	0.05	0.37
	Verbal episodic memory	Penn Word Memory Test	−0.07	0.05	0.21
	Working memory	List Sorting Working Memory Test	−0.04	0.06	0.50
	Fluid cognition	Dimensional Change Card Sort Test, Flanker, Picture Sequence Memory, List Sorting, and Pattern Comparison measures	0.12	0.07	0.10
	Early childhood cognition	Picture Sequence Memory, Dimensional Change Card Sort Test, Flanker, and Picture Vocabulary	0.14	0.08	0.07
	Cognitive function	All NNIH Toolbox Cognition measures	0.12	0.08	0.13
	Crystallized cognition	Picture Vocabulary and Reading Recognition measures	0.10	0.07	0.18
Emotion	Emotion recognition	Penn Emotion Recognition Test	0.01	0.05	0.91
	Anger	Anger-Affect Survey	0.68	0.03	<0.001*
	Hostility and cynicism	Anger-Hostility Survey	0.56	0.03	<0.001*
	Aggression	Anger-Physical Aggression Survey	0.33	0.04	<0.001*
	Fear and anxious misery	Fear-Affect Survey	0.67	0.03	<0.001*
	Somatic symptoms of anxiety	Fear-Somatic Arousal Survey	0.34	0.04	<0.001*
	Sadness	Sadness Survey	0.74	0.02	<0.001*
	Life satisfaction	General Life Satisfaction Survey	−0.58	0.04	<0.001*
	Meaning and purpose	Meaning and Purpose Survey	−0.55	0.04	<0.001*
	Positive affect	Positive Affect Survey	−0.61	0.04	<0.001*
	Friendship	Friendship Survey	−0.56	0.04	<0.001*
	Loneliness	Loneliness Survey	0.71	0.03	<0.001*
	Hostility	Perceived Hostility Survey	0.55	0.03	<0.001*
	Rejection	Perceived Rejection Survey	0.68	0.03	<0.001*
	Emotional support	Emotional Support Survey	−0.63	0.04	<0.001*
	Instrumental support	Instrumental Support Survey	−0.47	0.04	<0.001*
	Stress	Perceived Stress Survey	0.75	0.02	<0.001*
	Self-efficacy	Self-Efficacy Survey	−0.45	0.04	<0.001*
Motor	Endurance	2 min walk test	0.00	0.05	0.98
	Locomotion	4-meter walk test	−0.04	0.04	0.40
	Dexterity	9-hole Pegboard	−0.10	0.05	0.03
	Strength	Grip Strength Dynamometry	−0.03	0.04	0.39
Personality	Agreeableness	Five Factor Model	−0.41	0.04	<0.001*
	Openness	Five Factor Model	−0.01	0.05	0.80
	Conscientiousness	Five Factor Model	−0.39	0.04	<0.001*

Table 1 (continued) | Behavioral measures of the HCP cohort (n = 991)

Domain	Subdomain	Measure Name	CC	SD	p
	Neuroticism	Five Factor Model	0.64	0.03	<0.001*
	Extraversion	Five Factor Model	−0.43	0.04	<0.001*
Sensory	Audition	Words in Noise	0.06	0.05	0.23
	Olfaction	Odor Identification Test	0.10	0.04	0.01
	Pain	Pain Intensity and Interference Surveys	0.27	0.04	<0.001*
	Taste	Regional Taste Intensity Test	0.03	0.04	0.46
	Contrast sensitivity	Mars Contrast Sensitivity	−0.03	0.02	0.21

The correlation coefficient (CC) denotes Pearson's correlation between participants' behavioral measures and their behavioral composite scores. These correlations show the contribution of each behavioral measure to the first latent component, along with their bootstrap-estimated standard deviations (SD). The p-values were corrected by FDR and were determined based on one-sided tests. Asterisk indicates correlations with significant bootstrapped Z scores ($p_{FDR} < 0.05$).
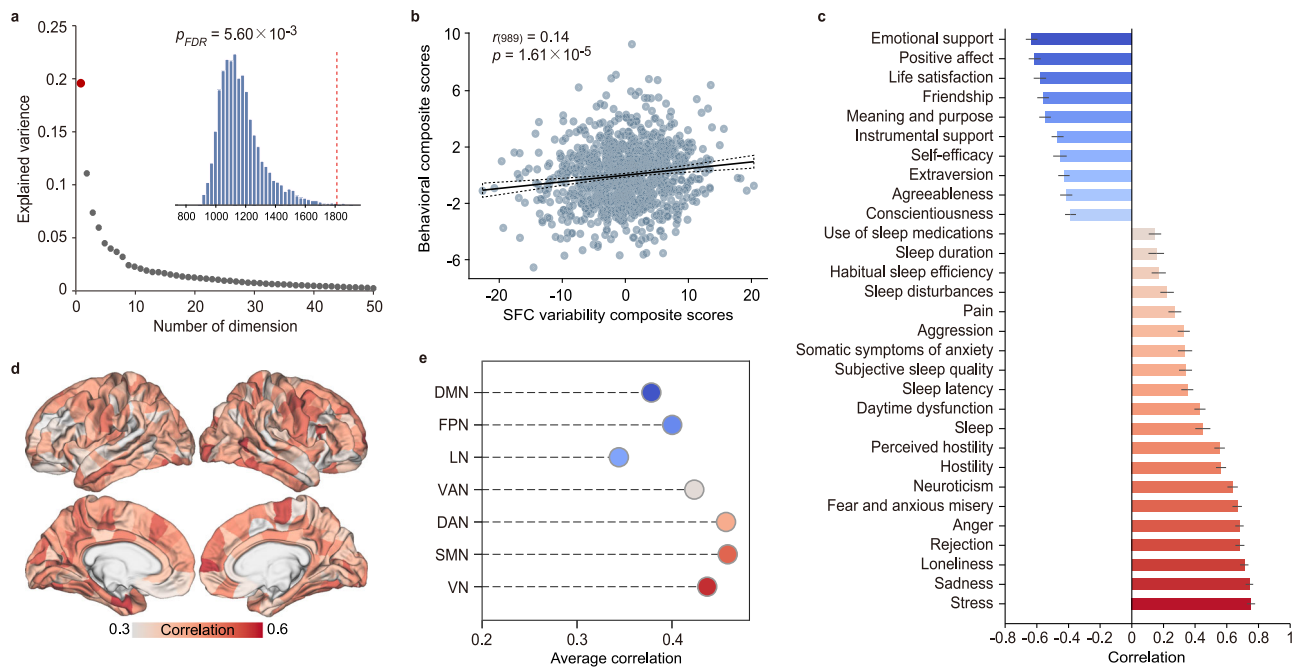
Fig. 4 | SFC variability represents a composite dimension of the emotion domain. a The amount of covariance accounted for by each latent component. After conducting permutation testing with FDR correction, only the first latent component remained statistically significant ($n = 5000$, $p_{FDR} = 5.60 \times 10^{-3}$, one-sided), which explained 19.42% of SFC variability-behavior covariance. **b** Significant association between behavioral and SFC variability composite scores in the first latent component (Pearson's $r_{(989)} = 0.14$, two-sided, $p = 1.61 \times 10^{-5}$). **c** Associations between behavioral composite scores and the corresponding behavioral traits. Error bars denote bootstrapped standard deviation with 1000 bootstrap estimations ($n = 1000$). The correlation coefficients were divided by their estimated standard deviation to calculate the Z-scores, which were further transformed into p-values and adjusted for multiple comparisons using the FDR correction ($p_{FDR} < 0.05$). **d** Significant associations between SFC variability composite scores and the corresponding SFC variability distribution. The correlation coefficients were divided by their estimated standard deviation to calculate the Z-scores, which were further transformed into p-values and adjusted for multiple comparisons using the Bonferroni correction ($p < 0.001$). **e** Associations between SFC variability composite scores and the SFC variability distribution that averaged within Yeo 7 functional subnetworks. Source data are provided as a Source Data file.
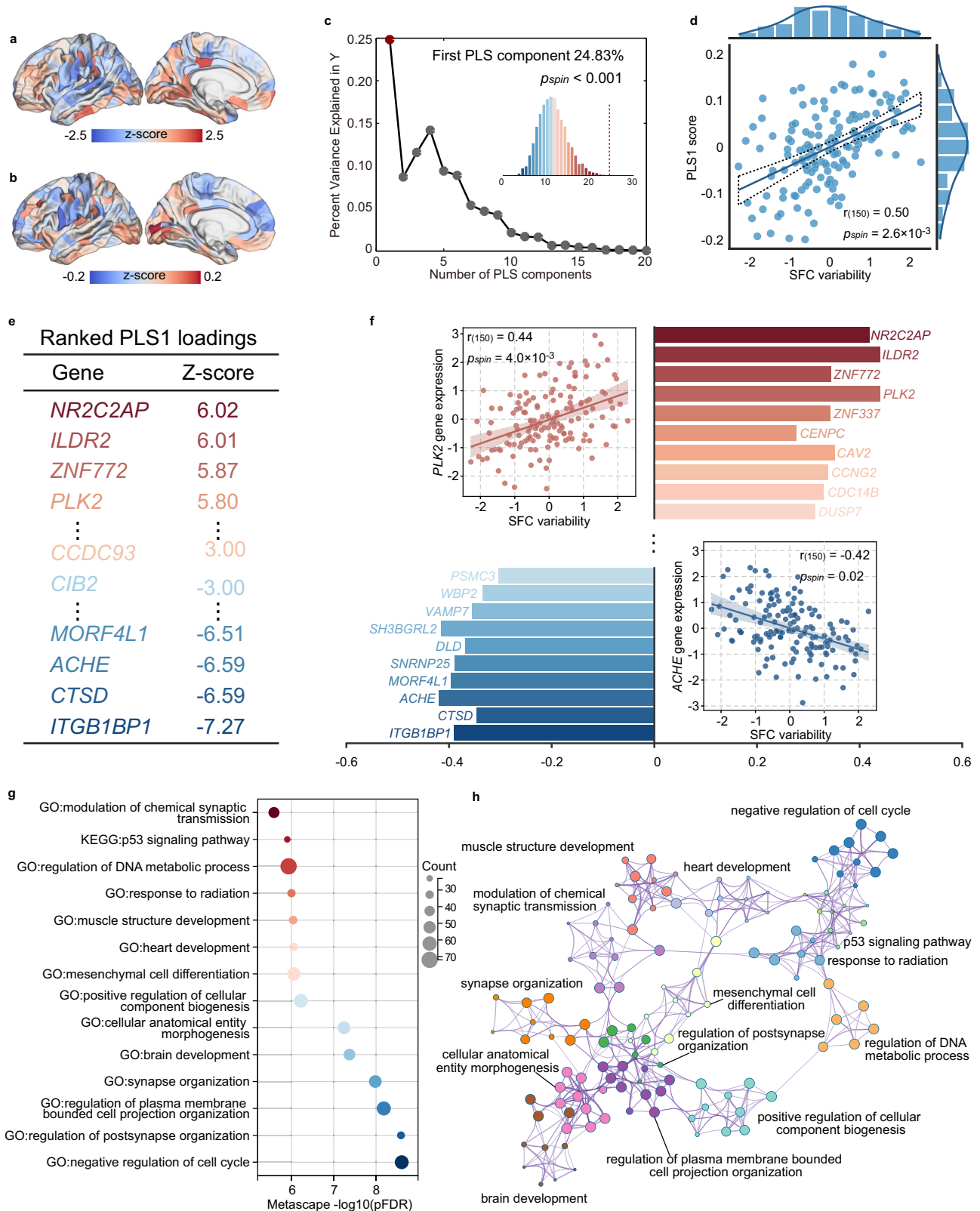
behavioral traits are reported in Table 1. Specifically, the first latent component's behavioral composite score was most associated with individual emotion domains, including social relationships (stress, emotional support, friendship, loneliness, rejection), negative affect (sadness, anger, fear, and anxious misery), and psychological well-being (life satisfaction, meaning, and purpose). Namely, a higher behavioral composite score was linked to poorer emotional status, such as perceived stress, sadness, loneliness, perceived rejection, anger, fear, and anxious misery. Figure 4d shows regions exhibiting significant correlations between the first latent component's SFC variability composite scores and the SFC variability distribution ($p < 0.001$, Bonferroni corrected). This indicates that a higher SFC variability composite score is associated with increased SFC variability, which is widely distributed throughout the brain. Uncorrected

correlations between participants' SFC variability distribution and their SFC variability composite scores are exhibited in Supplementary Fig. S3. Figure 4e displays the average correlations of significant SFC variability within subnetworks. A higher SFC variability composite score was found to be related to elevated levels of SFC variability in the DAN, SMN, and VN. Supplementary Table S1 further presents the top 20 ROIs with the highest correlations, localized at the fusiform, precentral, paracentral, postcentral, and superior parietal gyrus that consistently clustered within the SMN, DAN, and VN.

Transcriptomic decoding of cortical SFC variability

Gene expression plays an essential role in shaping the functional and structural organization of the cerebral cortex[17]; however, it remains unclear whether the topologically distinctive and functionally

e Ranked PLS1 loadings

| Gene	Z-score
NR2C2AP	6.02
ILDR2	6.01
ZNF772	5.87
PLK2	5.80
⋮	⋮
CCDC93	3.00
CIB2	-3.00
⋮	⋮
MORF4L1	-6.51
ACHE	-6.59
CTSD	-6.59
ITGB1BP1	-7.27

specialized SFC variability is associated with a unique transcriptional signature. To reveal this, we utilized the AHBA to obtain brain-wide patterns of gene expression (Fig. 5a) and conducted PLS regression analysis to detect the predominant gene expression organization. The first component of PLS (PLS1; Fig. 5b) depicted gene expression pattern that is mostly associated with cortical SFC variability distributions, which explained 24.83% of the variance in SFC variability ($p_{spin} < 0.001$;

Fig. 5c). Meanwhile, significant spatial association between the SFC temporal variability and the PLS1 was observed ($r_{(150)} = 0.50$, $p_{spin} = 2.6 \times 10^{-3}$; Fig. 5d). Furthermore, by utilizing a univariate one-sample Z test, we ranked these candidate genes based on normalized PLS1 weights, identifying 947 negatively (PLS1-: Z < -3, $p_{FDR} < 0.05$) and 835 positively weighted genes (PLS1 + : Z > 3, $p_{FDR} < 0.05$; Fig. 5e). Of note, genes exhibiting negative PLS weights displayed a negative

Fig. 5 | Transcriptomic decoding of cortical SFC variability. a Topographic distribution of cortical SFC variability in the left hemisphere. **b** Cortical distribution of regional PLS1 scores in the left hemisphere. **c** Explained variance for the first 20 components derived from the PLS regression analysis. The significance of the variance explained by each PLS component was assessed by the *spin* test ($n = 5000$, one-sided). **d** Correlation between cortical SFC variability and PLS1 scores (Pearson's $r_{(150)} = 0.50$, $p_{spin} = 2.6 \times 10^{-3}$). The *p*-value was not corrected for multiple comparisons and was determined based on a one-sided test. **e** Ranked PLS1 loading. **f** Genes exhibiting negative PLS weights displayed a negative spatial association between

their expressions and SFC variability map (e.g., *ACHE*: Pearson's $r_{(150)} = -0.42$, $p_{spin} = 0.02$), while those with positive PLS weights exhibited a positive association between their expressions and SFC variability map (e.g., *PLK2*: Pearson's $r_{(150)} = 0.44$, $p_{spin} = 4.0 \times 10^{-3}$). All *p*-values were derived from spin tests and adjusted by FDR, and were determined based on one-sided tests. **g** Enrichment analysis of genes transcriptionally associated with cortical SFC variability. All obtained pathways were adjusted for multiple comparisons using the FDR correction ($p_{FDR} < 0.01$). **h** The intra- and inter-cluster similarities of enriched terms are visualized by the Metascape enrichment network. Source data are provided as a Source Data file.
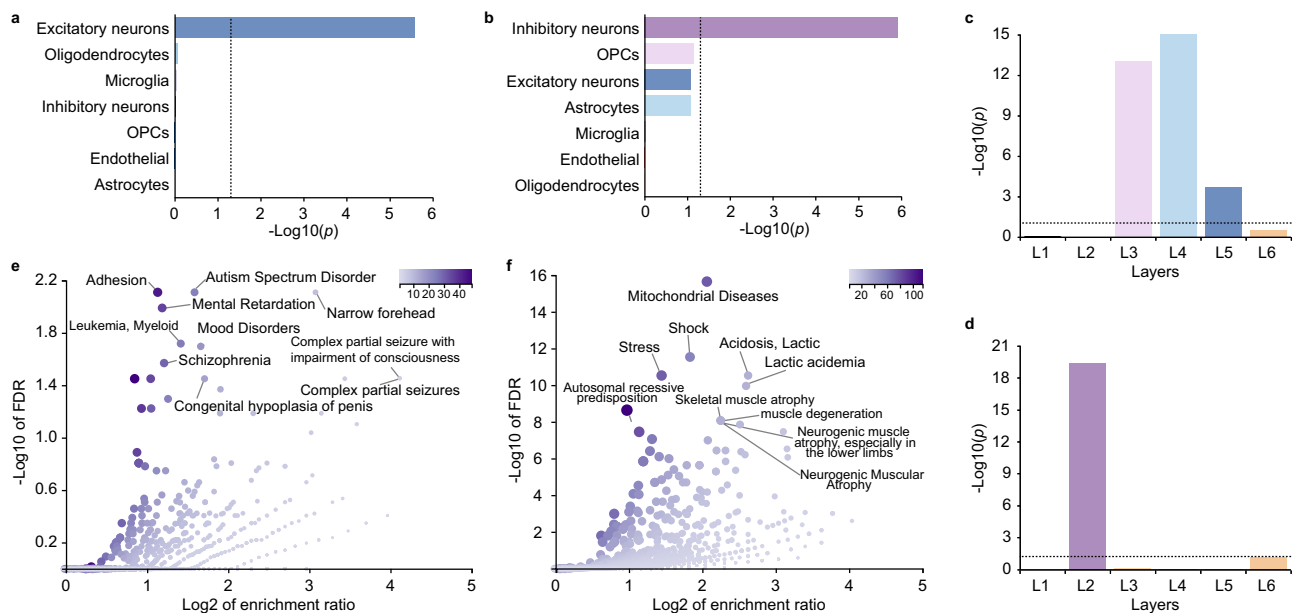
Fig. 6 | Cell type, cortical layer, and brain disease specificity of brain SFC variability. Overlap of cell-type specific genes and those exhibiting (**a**) positive and (**b**) negative PLS1 weights. OPCs-oligodendrocyte precursors. Overlap of cortical layer-related genes and those exhibiting (**c**) positive and (**d**) negative PLS1 weights.

All permutated p_{perm} values were adjusted by FDR, and were determined based on one-sided tests. Overlap of brain disease candidate genes and those exhibiting **e** positive and **f** negative PLS1 weights. Only the top 10 terms were annotated.

spatial association between their expressions and SFC variability map (e.g., *ACHE*: $r_{(150)} = -0.42$, $p_{spin} = 0.02$), while those with positive PLS weights exhibited a positive spatial association between their expressions and SFC variability map (e.g., *PLK2*: $r_{(150)} = 0.44$, $p_{spin} = 4.0 \times 10^{-3}$; Fig. 5f).

To explore the potential impact of molecular biological signatures on the distribution of cortical SFC variability, we utilized Metascape[29] to align PLS1+ and PLS1- genes with the Kyoto Encyclopedia of Genes and Genomes (KEGG) pathways and gene ontology (GO) biological processes, respectively. After adjusting for enriched terms ($p_{FDR} < 0.01$) and eliminating discrete enrichment clusters, the PLS1+ gene list exhibited significant enrichment in 13 GO biological processes (Fig. 5g, h), such as "regulation of postsynapse organization", "synapse organization", and "negative regulation of cell cycle", and one KEGG pathway "p53 signaling pathway". Supplementary Table S2 lists all GO Biological Process and KEGG Pathway enrichments from the PLS+ gene set. Additionally, the PLS1 gene list exhibited a significant enrichment in GO biological processes, including "mitochondrion organization", "peptide metabolic process", and "protein catabolic process", together with KEGG pathways, such as the "Carbon metabolism" and "Biosynthesis of cofactors" ($p_{FDR} < 0.01$; Supplementary Fig. S4 and Table S3).

SFC variability-related genes enriched for cell classes and cortical layers

We proceeded to investigate whether there was an enrichment of genes associated with specific cell types and cortical layers among

PLS + and PLS− genes. Firstly, we observed that genes with positive PLS1 weights were significantly expressed in excitatory neurons ($n = 120$, $p_{perm} < 0.001$; Fig. 6a). Concurrently, genes specific to inhibitory neurons ($n = 72$, $p_{perm} < 0.001$) were overrepresented in the PLS1- genes of cortical SFC variability (Fig. 6b). In line with above findings, enrichment analysis of these overlapped genes uncovered that cortical SFC variability was significantly enriched in biological processes associated with excitatory and inhibitory neurons (Supplementary Fig. S5). Thereafter, we associated the PLS1 gene list with distinct cortical layers by utilizing the laminar gene markers[30]. As illustrated in Fig. 6c, the PLS1+ genes exhibited a significant enrichment in layer III ($n = 41$, $p_{perm} < 0.001$), layer IV ($n = 44$, $p_{perm} < 0.001$), and layer V ($n = 21$, $p_{perm} < 0.001$), whereas the PLS1+ gene list showed a significant enrichment in layer II ($n = 48$, $p_{perm} < 0.001$).

SFC variability-related genes enriched for disease candidate genes

To assess the clinical relevance of genes linked to SFC variability, we further examined whether the PLS + and PLS− gene lists exhibited enrichment for those implicated in the pathogenesis of brain disease. To achieve this, the WebGestalt[31] was applied to the PLS1+ and PLS1− gene lists, respectively. The findings revealed a significant overlap between PLS1+ genes and those implicated in emotional disease, encompassing mood disorders, schizophrenia, and autism spectrum disorder (Fig. 6e). Additionally, significant overlap was also observed between genes associated with mitochondrial diseases and shock in relation to the PLS1- genes (Fig. 6f).
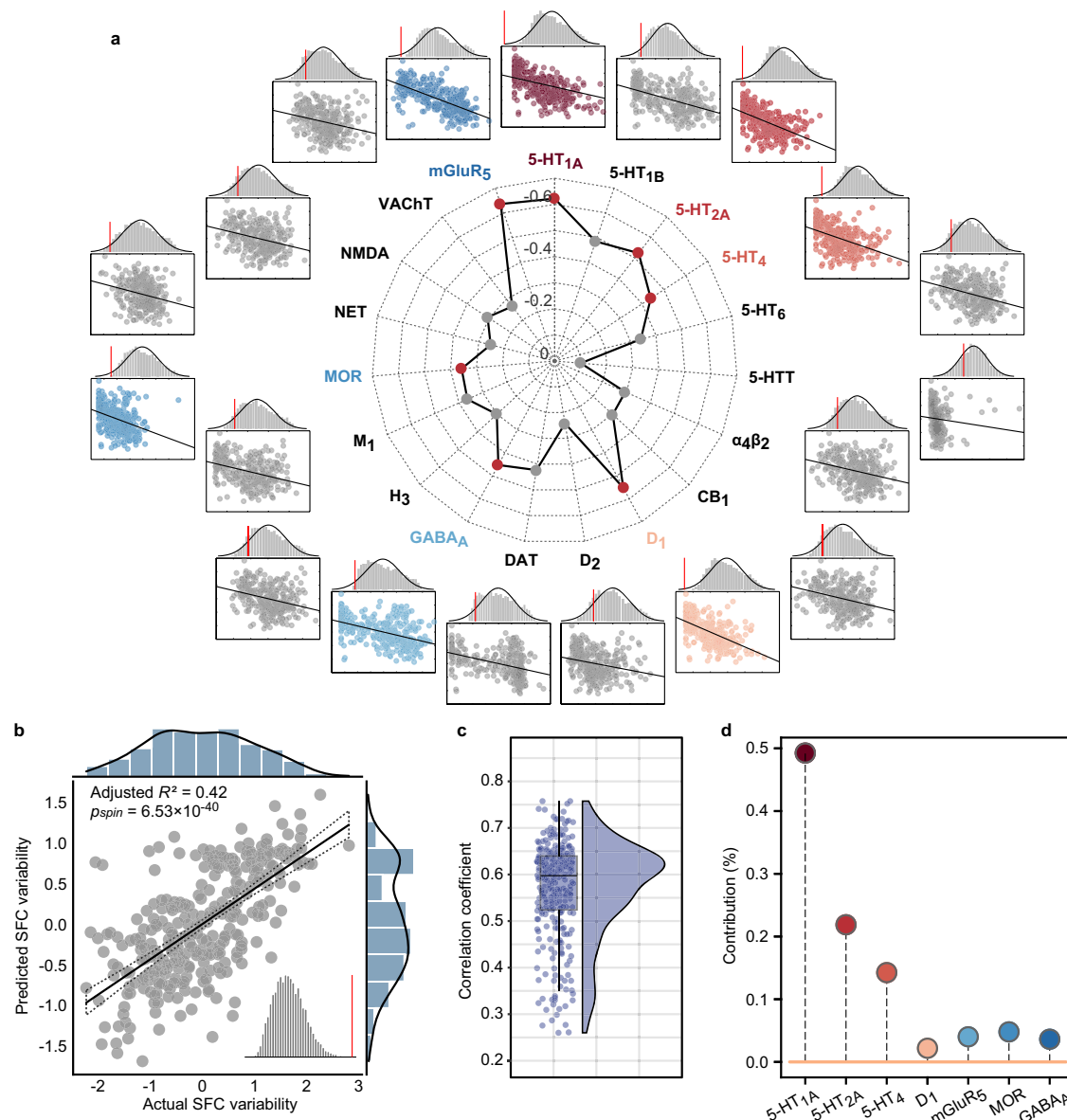
Fig. 7 | Relationship between neurotransmitter systems and brain SFC variability. a Relationship between each neurotransmitter map and cortical SFC variability. Histograms display the frequency distributions of correlation coefficients from 5000 permutation tests, with red bars indicating the actual Pearson's r-values. **b** Prediction of SFC variability based on brain receptor distributions (Adjusted $R^2 = 0.42$, $p_{spin} = 6.53 \times 10^{-40}$). The p-value was derived from the spin test and determined based on a one-sided test. **c** The distribution of Pearson's correlations between predicted and actual SFC variability using a distance-

dependent cross-validation method. This method selects the 75% of regions closest to a source region as a training set and the remaining 25% of regions as the test set, for a total of 308 repetitions. Boxplots represent the median and upper/lower quartile with whiskers extending to the most extreme data point within 1.5 interquartile ranges above/below the quartiles. **d** Dominance analysis. The contribution percentage per neurotransmitter was determined by normalizing its dominance in relation to the overall model fit (adjusted R^2). Source data are provided as a Source Data file.

Relationship between SFC variability and neurotransmitter systems

To obtain brain neurotransmitter receptor densities, we compiled PET scans of 9 neurotransmitter systems, encompassing opioid, cannabinoid, histamine, γ-aminobutyric acid (GABA), glutamate, acetylcholine, serotonin, norepinephrine, and dopamine (Supplementary Table S4)[19]. A tracer map was generated by averaging the data from participants within each PET study, which was then segmented into the D-K atlas and subsequently standardized using z-scores. Spatial correlations between brain SFC variability and neurotransmitter receptor distributions were examined. After the "*spin*"-based spatial permutation testing with FDR correction, we observed that SFC temporal variability was significantly

negatively related to serotonin receptors (5-HT$_{1A}$: $r_{(306)} = -0.62$, $p_{spin\text{-}FDR} < 0.001$, 5-HT$_{2A}$: $r_{(306)} = -0.52$, $p_{spin\text{-}FDR} < 0.001$) and transporters (5-HTT: $r_{(306)} = -0.44$, $p_{spin\text{-}FDR} < 0.001$), together with metabotropic glutamate receptor 5 (mGluR$_5$: $r_{(306)} = -0.55$, $p_{spin\text{-}FDR} < 0.001$), GABA type A (GABA$_A$: $r_{(306)} = -0.45$, $p_{spin\text{-}FDR} = 0.001$) receptor, dopamine (D$_1$: $r_{(306)} = -0.55$, $p_{spin\text{-}FDR} < 0.001$), and μ-opioid receptor (MOR: $r_{(306)} = -0.55$, $p_{spin\text{-}FDR} = 0.001$) in Fig. 7a. Detailed statistical result of each neurotransmitter map with SFC variability are reported in Supplementary Table S5.

Thereafter, employing a multiple linear regression model, we tested whether neurotransmitter receptor and transporter densities (i.e., 5-HT$_{1A}$, 5-HT$_{2A}$, 5-HT$_4$, D$_1$, mGluR$_5$, MOR, and GABA$_A$) could serve as predictors for the cortical distribution of SFC variability. The

model significance was evaluated by a "*spin*"-based permutation test (5000 repetitions). Figure 7b exhibits a close and statistically significant fit between cortical SFC variability and 5-HT$_{1A}$, 5-HT$_{2A}$, 5-HT$_4$, D$_1$, mGluR$_5$, GABA$_A$, and MOR densities (Adjusted $R^2 = 0.42$, $p_{spin} = 6.53 \times 10^{-40}$). Next, we cross-validated the regression model using a distance-dependent method[32]. The distribution of Pearson's correlations for 308 out-of-sample cross-validations is shown in Fig. 7c. The median of the cross-validated Pearson's correlation between the predicted and actual SFC variability was $r = 0.60$. Additionally, dominance analysis[33] was adopted to identify the relative contribution of each neurotransmitter receptor/transporter towards the overall model fit. Results in Fig. 7c demonstrate that the spatial distribution of the serotonin neurotransmitter system, encompassing 5-HT$_{1A}$, 5-HT$_{2A}$, and 5-HT$_4$, largely contributes (over 85%) to the fit between neurotransmitter systems and cortical SFC variability.

Robustness and sensitivity analyses

We further validated the cortical SFC variability pattern and its underlying transcriptional relations in another independent cohort, i.e., the CHCP cohort. Firstly, the spatial agreement between the SFC variability map derived from the CHCP cohort (Fig. 8a) and that of the HCP cohort was observed ($r_{(306)} = 0.64$, $p_{spin} = 2.15 \times 10^{-37}$; Fig. 8b). PLS regression was then performed to validate the transcriptional enrichments of the SFC variability map. The findings reveal that PLS1 (Fig. 8c) accounted for 20.77% of the variance in SFC variability of the CHCP cohort ($p_{spin} = 0.001$), close to that of the HCP cohort. Likewise, significant spatial coherency between the PLS1 and cortical SFC variability in the CHCP cohort was observed ($r_{(150)} = 0.46$, $p_{spin} < 0.001$; Supplementary Fig. S6). In addition, 646 positively weighted genes (PLS1 +, Z > 3) and 891 negatively weighted genes (PLS1-, Z <− 3) were identified in the CHCP cohort. Then, using a multi-gene-list meta-analysis[29], we validated that the enrichment pathways on PLS1+ (PLS−) genes derived from the 2 independent cohorts were highly overlapped. The shared ontology terms for PLS1+ genes primarily focused on "regulation of postsynapse organization", "synapse organization", and "negative regulation of cell cycle" etc. (Fig. 8d). Additionally, the PLS1− genes of both HCP and CHCP cohorts were consistently enriched for GO biological processes including "mitochondrion organization", "peptide metabolic process", and "protein catabolic process", together with KEGG pathways, such as the "Carbon metabolism" and "Biosynthesis of cofactors" (Fig. 8e).

Eventually, we performed sensitivity analyses to evaluate whether our results would be robust under several methodologies. Firstly, given that brain structural organization can also be evaluated using white matter network (WMN) and microstructural profile covariance network (MPCN)[34], WMN- and MPCN-derived SFC variability were also estimated. As exhibited in Supplementary Results 2 and Fig. S7, WMN-derived SFC variability demonstrated a significantly moderate degree of spatial correlation with MSN-derived SFC variability ($r_{(306)} = 0.43$, $p_{spin} < 0.001$). Then, PLS was applied to examine the multivariate relationships between WMN-derived SFC variability and behavioral measures. As shown in Supplementary Results 2 and Fig. S8, beyond the emotion domain, the first latent component's behavioral composite score exhibited stronger associations with cognition and alertness. When further employing PLS regression to examine the relationship between WMN-derived SFC variability and transcriptomic variations, none of the PLS components reached statistical significance ($p_{spin} > 0.05$; Supplementary Results 2 and Table S6).

As for MPCN-derived SFC variability, Supplementary Results 3 demonstrated a spatial distribution (Supplementary Fig. S9) and behavioral covariance (Supplementary Fig. S10) that were more closely aligned with MSN-derived SFC variability. When further investigating transcriptome-neuroimaging associations, the PLS1 can explain 16% of the variance in MPCN-derived SFC variability ($p_{spin} = 0.02$; Table S7). Moreover, using a multi-gene-list meta-analysis[29], we observed that the gene lists and enrichment pathways of MPCN- and MSN-derived SFC variability were highly overlapping (Supplementary Fig. S11).

Although the tvSFC was calculated based on morphometric similarity and functional profiles of the same region, edge-level spatial proximity can lead to artificially inflated SFC values for regions that are closer to others. As previously demonstrated, fuzzy entropy is insensitive to the data magnitude but rather depends more on the data distribution[11], enabling it to effectively capture the intrinsic dynamic fluctuation patterns of a given time series, thereby can effectively mitigating the consistent impact of edge-level spatial proximity on the magnitude of SFC across all time points. To further validate this, following previous studies[35,36], we calculated tvSFC by utilizing the partial correlation between morphometric similarity and functional co-fluctuation connectivity, while regressing the shared relationship with anatomical distance. Fuzzy entropy was then applied to generate the SFC variability distribution. As expected, SFC temporal variability maps with and without regression of Euclidean distance exhibited extremely strong spatial consistency ($r_{(306)} = 0.98$, $p_{spin} < 0.001$; Supplementary Result 4 and Fig. S12).

Discussion

Our multimodal investigation of complex functional dynamics that unfold over the intrinsic structural backbone illuminates how the temporal variability of cortical SFC was supported by transcriptomic and cellular substrates, as well as chemoarchitecture, to facilitate neurocognitive processing. Specifically, leveraging time- and region-resolved SFC coupling patterns, we quantified how much cortical SFC dynamically fluctuates over time, reflecting its temporal variability. We then provided converging evidence highlighting the crucial role of cortical SFC variability in the domain of brain emotion, and additionally elucidated its neurobiological underpinnings at multiple levels by integrating transcriptomic, cellular, and neurotransmitter evidence. Our discoveries offer a new outlook on the temporal variability of dynamic SFC in brain function, with underlying implications for comprehending cognitive processes and diseases at both macroscopic architectural and microscopic transcriptomic levels.

By introducing fuzzy entropy to quantify the degree of dynamic SFC fluctuation over time, we revealed that SFC temporal variability is highly heterogeneous. Specifically, the prefrontal and occipital gyrus exhibited more sizable SFC fluctuations that clustered mainly in visual and limbic subsystems; while SFC of the dorsal and ventral attention subsystems, which dispersed in extensive frontal and parietal regions, were more stable over time. More interestingly, we revealed that a composite emotion domain, encompassing social relationships, negative affect, and psychological well-being, was particularly associated with the spatial pattern of cortical SFC variability in widespread fusiform, precentral, paracentral, postcentral, and superior parietal gyrus within the SMN, DAN, and VN subsystems. As reported, the fusiform and precentral gyrus play crucial roles in processing emotional information[37,38]. Meanwhile, emotion and action mutually interact with each other in a crucial way, as evidenced by functional neuroimaging research investigating how emotions influence brain regions associated with motor functions. For example, Portugal et al[39]. discovered that motor-related regions, such as the precentral gyrus, exhibit context-dependent activation when processing emotional stimuli. In addition, attention modulates emotion and related systems such as face recognition and reward[40]. Both the involvement of spatial attention and feature-based attention in the dorsal attention network are essential for emotion regulation[41].
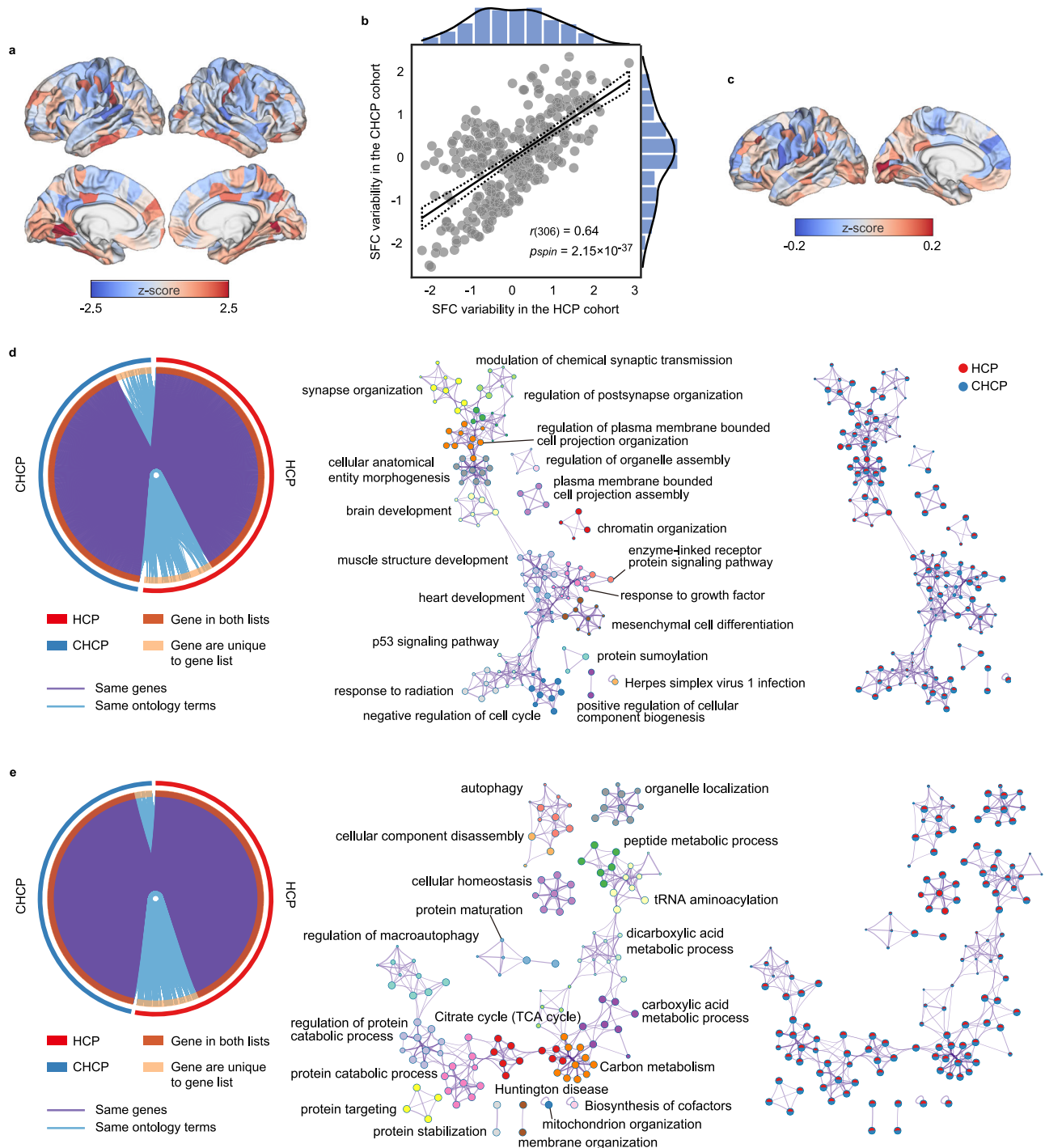
Fig. 8 | Reproducibility of SFC variability and corresponding transcriptomic profile. a Cortical SFC variability map in the CHCP cohort. **b** Pearson's correlation analysis for 308 regions of D-K atlas between HCP and CHCP cohorts (Pearson's $r_{(306)} = 0.64$, $pspin = 2.15 \times 10^{-37}$, one-sided). **c** Weighted gene expression map of PLS1 for the CHCP cohort. **d** Validation of transcriptional enrichments of SFC variability with PLS1+ weights. **e** Validation of transcriptional enrichments of SFC variability with PLS1− weights. Circos plot depicting the overlap of genes between HCP and CHCP cohort. Source data are provided as a Source Data file.

Thereafter, transcriptome signatures were unveiled by leveraging the intricate topographic distribution of brain SFC temporal variability. As illustrated, brain genes exhibited differential expression in regions characterized by varying degrees of temporal variability, wherein genes with overexpression in regions displaying high temporal variability (PLS1+) showed enrichment for terms associated with synapses including "regulation of postsynapse organization" and "synapse organization", as well as cell cycle-related biological processes including "negative regulation of cell cycle" and

"regulation of DNA metabolic process". In fact, the classic mechanism for neural cell communication in the central nervous system is represented by synapses. Synaptic transmission necessitates intricate structural specializations in both postsynaptic and presynaptic cells, while the dynamic architecture of synapses allows for highly modifiable signal transmission[42]. Thus, genes enriched for synapse-related terms may result in and reshape the highly regionally specialized SFC variability. In addition, the regulation of cellular metabolism during cell cycle progression may hold profound implications

for understanding the biology of highly specialized cell types. The regulation of the cell cycle exerts critical control over region-specific rates of neuronal generation and the formation of cytoarchitectonic maps[43]. In this regard, our results consistently reveal that SFC variability is specifically related to genes overexpressed in excitatory neurons of cortical layers III, IV, and V. In fact, the mediation of intricate emotional changes heavily relies on excitatory transmission, which may represent the ultimate shared pathway for therapeutic interventions targeting mood disorders[44]. Meanwhile, disruption of synaptic communication is closely linked to emotional disturbances observed in neurological conditions such as schizophrenia, depression, and autism[45]. As such, the clinical significance of PLS1+ genes further demonstrated that genes enriched for synapse- and cell-cycle-related biological processes were related to multiple emotion-related diseases, including mood disorders, schizophrenia, and autism spectrum disorder.

On the other hand, the PLS1− gene list exhibited enrichment in multiple KEGG pathways and GO biological processes, including "mitochondrion organization", "regulation of mitochondrion organization", "carbon metabolism", and "cellular homeostasis". As we know, mitochondria play a crucial role in ensuring survival. Apart from their role in energy metabolism, mitochondria also play a vital part in various biochemical and signaling pathways essential for maintaining brain homeostasis, such as metabolic pathways, cellular signaling, generation of free radical species, apoptosis, and lipid synthesis[46]. In particular, mitochondria are commonly acknowledged as key players in facilitating allostasis, which refers to the intricate interplay among autonomic, metabolic, and immune systems to maintain cellular homeostasis under stressful conditions[47]. Meanwhile, considering its crucial function within the human body, abnormalities in mitochondrial performance can lead to catastrophic outcomes. It is well known that deleterious mutations in mitochondrial genes could lead to mitochondrial diseases, in which epilepsy often occurs as one of the main clinical features[48]. Hence, when exploring the enrichment analysis of brain disease, the PLS1− genes overexpressed in low SFC variability areas consistently and significantly overlapped with the genes associated with mitochondrial diseases, stress, and shock.

The distribution of neurotransmitter receptors and transporter molecules across the cortical mantle, known as chemoarchitecture, is an equally crucial facet of brain neurobiology alongside cellular composition. The level and functional status of neurotransmitters will, in turn, affect the connection pattern and information transfer efficiency between brain structures by modulating neuronal excitability, thereby potentially playing a key role in the dynamic fluctuations of SFC. As expected, spatial correlation analyses demonstrated a significant association between SFC variability and cortical receptor distribution, suggesting that the interplay between structural and functional aspects heavily relies on the underlying chemoarchitecture[20]. More importantly, our study reveals that cortical SFC variability can be attributed to the overlapping distributions of various neurotransmitter systems, including serotonin (55-HT$_{1A}$, 5-HT$_{2A}$, 5-HT$_4$), glutamate (mGluR$_5$), GABA (GABA$_A$), and opioid (MOR). This observation aligns with the notion that the cortical receptome exhibits similar organizational characteristics to those found in brain functional and structural anatomy[20]. In fact, the previous study has identified the simultaneous release of multiple neurotransmitters[49]. For instance, the synaptic flexibility can be significantly enhanced when GABA is released in conjunction with other co-transmitters like glutamate[50]. Moreover, neurotransmitter receptors drive neuronal excitability and synaptic plasticity, shape network-wide communication, and modify neural states that are underpinned by intrinsic anatomy[51], thereby potentially regulating the temporal variability of brain SFC.

As demonstrated, the proposed SFC variability method exhibits robustness across various structural measurement techniques, provided that inter-regional structural relationships are reliably quantified. However, due to several long-standing technical limitations[52,53], WMN might not be ideal for whole-brain connectome mapping, thereby resulting in the suboptimal estimation of SFC variability as demonstrated. Although MPCN- and MSN-derived SFC variability yield highly consistent results, future research should be guided by the specific hypothesis under investigation when choosing between MSN and MPCN for estimating SFC variability. Specifically, MSN is well-suited for investigating structural organizations characterized by multimodal macrostructural MRI phenotypes, whereas MPCN is more appropriate for studies hypothetically motivated by lamina-specific aspects of cortical architectonics and connectivity[54]. Additionally, in contrast to time-varying network analysis[55], which examines the formation, dissolution, or reconfiguration of inter-regional functional interactions at an arbitrarily high temporal resolution, the temporal variability approach primarily focuses on quantifying the extent to which moment-to-moment neural activity fluctuates. Temporal variability analysis emphasizes within-region signal dynamics while time-varying network analysis focuses on between-region interaction dynamics. These two methods offer complementary perspectives for advancing neuroscience research. Moreover, the temporal variability method can also be extended for application in task-related states. Specifically, when the temporal resolution of functional signals is sufficiently high (e.g., electroencephalogram), this method can capture single-trial variability under a given stimulus condition. For fMRI, which exhibits relatively lower temporal resolution, this method can still be adapted to assess trial-to-trial brain variability across repeated task blocks.

Our study had several limitations. First, the correlation between behavioral and SFC variability composite scores in the first latent component is generally weak, and the interpretability of the PLS results should be taken with caution. In addition, since the behavioral data in the CHCP database are not publicly accessible, it is not feasible to conduct further verification of the behavioral PLS results. In future works, more effort will be put into further validating our findings, as well as improving the generalization of these multivariate relationships between SFC variability and behavioral measures. Second, considering that significant genes were identified not through correlations with spatially defined phenotypes but via a multivariate PLS framework, the strategy proposed by Fulcher et al[56]., which is robust for addressing spatial autocorrelation biases in gene category enrichment analysis, may not be fully applicable[57]. In this regard, it remains uncertain whether such bias influences the current results, thereby underscoring the need for future research to develop methods capable of addressing this issue.

Methods
Participants
This study enrolled 1206 unrelated participants from the S1200 release of HCP[21]. We then excluded participants if the following data were unavailable: a complete sMRI scan, dMRI scan, and 3 T resting-state fMRI scan. The CHCP cohort[22] included 366 native Chinese healthy participants with complete multimodal neuroimaging data. The HCP and CHCP cohorts obtained approval from the Institutional Review Board of Washington University and Peking University, respectively. All participants provided their written informed consent. After quality control, 991 participants in the HCP cohort and 318 participants in the CHCP cohort with complete multimodal neuroimaging data were retained. Please refer to Supplementary Fig. S13 for the participant numbers corresponding to each stage of the study. The demographic characteristics of all included participants are provided in Supplementary Table S8.

Multimodal data acquisition

Participants in the HCP cohort underwent scanning on a 3 T MR scanner equipped with a standard head coil consisting of 32 channels (Connectome Skyra, Siemens, Germany). The CHCP cohort's MRI scans were obtained using a 3 T Siemens Prisma scanner. Please refer to Supplementary Tables S9 and S10 for the detailed MRI acquisition parameters of both cohorts. In addition, the HCP data acquisition protocols are available at the HCP S1200 Release Manual[58], while those of the CHCP cohort are available in[22].

MRI preprocessing

Using FreeSurfer v6.0, we preprocessed the sMRI scans in surface-based space. Specifically, we reconstructed the cortical surface by skull stripping, brain tissue segmentation, separation of hemispheres and subcortical structures, as well as construction of gray/white interfaces and pial surfaces[59,60]. The dMRI was preprocessed utilizing the FMRIB Software Library v6.0 (FSL v6.0)[61] package. Firstly, the dMRI scans were subjected to correction for distortions caused by eddy currents and head movement. Subsequently, the diffusion tensor model was estimated utilizing a linear least-squares fitting approach.

The Data Processing & Analysis of Brain Imaging v7.0 (DPABI v7.0) toolkit was employed for the pre-processing of fMRI scans. Briefly, following the exclusion of the first ten scans, the remaining fMRI images underwent correction for time differences and head motion. Afterward, fMRI scans were subjected to spatial normalization for alignment with the standard MNI space. Next, images were resliced into a resolution of $2 \times 2 \times 2\,mm^3$ and underwent additional pre-processing steps including spatial smoothing (6 mm full-width at half-maximum), linear detrending, nuisance signal regression, and 0.01–0.1 Hz band-pass filtering. Finally, sixty-three participants of the HCP cohort and forty-eight participants in the CHCP cohort were discarded due to large head movement (rotation > 3.0° or translation > 3.0 mm).

Morphometric similarity network construction

For MSN construction, we first extracted nine morphometric characteristics from the preprocessed sMRI and dMRI scans based on the D-K atlas[23]. These features include curved index, folding index, mean diffusivity, fractional anisotropy, Gaussian curvature, gray matter volume, surface area, mean curvature, and cortical thickness. Subsequently, z-normalization was performed on each morphometric feature vector across ROIs, followed by the application of Pearson's correlations to the combined morphometric feature vector for paired ROIs, resulting in the generation of a participant-specific $MSN \in \mathbb{R}^{308 \times 308}$ as,

$$
MSN = \begin{bmatrix} p_{1,1} & p_{1,1} & \cdots & p_{1,308} \\ p_{2,1} & p_{2,2} & \cdots & p_{2,308} \\ \vdots & \vdots & \cdots & \vdots \\ p_{308,1} & p_{308,2} & \cdots & p_{308,308} \end{bmatrix} \quad (1)
$$

where $p_{i,j}$ is Pearson's correlation coefficient between the morphometric feature vector of ROI i and ROI j.

Estimation of time-varying SFC

Herein, time series for 308 ROIs of the D-K atlas were extracted based on preprocessed fMRI images. The average fMRI signals within each ROI were computed at each time point. Assuming that $x_i = \{x_i(1), x_i(2), ..., x_i(N)\}$ is the fMRI time series of ROI i, where $1 \le i \le 308$, and N denotes the number of sampling points. We subsequently z-scored the fMRI signals as z_i, while estimating the edge time series matrix $E \in \mathbb{R}^{308 \times 308 \times N}$ by performing element-wise product of pairwise signals[9] as,

$$
E = \begin{bmatrix} e_{1,1}(n) & e_{1,2}(n) & \cdots & e_{1,308}(n) \\ e_{2,1}(n) & e_{2,2}(n) & \cdots & e_{2,308}(n) \\ \vdots & \vdots & \cdots & \vdots \\ e_{308,1}(n) & e_{308,2}(n) & \cdots & e_{308,308}(n) \end{bmatrix}
$$
$$
= \begin{bmatrix} z_1(n)z_1(n) & z_1(n)z_2(n) & \cdots & z_1(n)z_{308}(n) \\ z_2(n)z_1(n) & z_2(n)z_2(n) & \cdots & z_2(n)z_{308}(n) \\ \vdots & \vdots & \cdots & \vdots \\ z_{308}(n)z_1(t) & z_{308}(n)z_2(n) & \cdots & z_{308}(n)z_{308}(n) \end{bmatrix} \quad (2)
$$

where $e_{i,j}$ indicates the element-wise product between edge time series z_i and z_j, n is the sampling time point, $n = 1, ..., N$.

Thereafter, each column in the MSN matrix, i.e., $p_{[:, i]}$, indicating an area's morphometric similarity connectivity to the remaining brain areas, was correlated (using Pearson's correlation) with the identical area's column in the functional co-fluctuation profile at time point n, i.e., $e_{[:, i]}(n)$, providing a time-varying SFC (tvSFC) $\in \mathbb{R}^{308 \times N}$ for each participant as,

$$
tvSFC = \begin{bmatrix} w_1^{pe}(n) \\ w_2^{pe}(n) \\ \vdots \\ w_{308}^{pe}(n) \end{bmatrix} \quad (3)
$$

where $w_i^{pe}(n)$ indicate the Pearson's correlation coefficient between $p_{[:, i]}$ and $e_{[:, i]}$ of the i-th ROI at the sampling time point n, $n = 1, ..., N$. This procedure finally generates a region × time matrix that captures the dynamic fluctuation of SFC for individual regions across time.

Temporal variability of cortical dynamic SFC

To evaluate the dynamic fluctuating degree of resting-state SFC over time, herein, the fuzzy entropy was applied to assess the complexity of these tvSFC series[11]. Concretely, assuming that each subject has N SFC, the series W_u ($1 \le u \le N$) for tvSFC per ROI can be expressed as,

$$
W_u^q = \{w(u), w(u+1), ..., w(u+q-1)\} - \overline{w}(u), u = 1, ..., N-q+1 \quad (4)
$$

where W_u^q denotes q consecutive w values of the u-th SFC point, which is determined by eliminating the baseline $\overline{w}(u) = q^{-1} \sum_{l=0}^{q-1} w(u+l)$.

The similarity index D_{ul}^q between W_u^q and the adjacency vector W_l^q for a given r can be calculated as,

$$
D_{ul}^q = \mu(d_{ul}^q, r) \quad (5)
$$

where d_{ul}^q denotes the largest absolute difference in the scalar components between W_u^q and W_l^q.

For each vector W_u^q ($u = 1, 2, ..., N-q+1$), by averaging all similarity degrees, D_{ul}^q, of its neighboring vectors W_l^q ($l = 1, 2, ..., N-q+1$, and $l \neq u$), we then get,

$$
\phi_u^q(r) = (N - q - 1)^{-1} \sum_{l=1, l \neq u}^{N-q} D_{ul}^q \quad (6)
$$

Based on $\varphi^m(r) = (N - q)^{-1} \sum_{u=1}^{N-q} \phi_u^q(r)$, the $FuzzEn(q, r)$ of W_u ($1 \le u \le N$) is defined as,

$$
FuzzEn(q, r) = \lim_{N \to \infty} [\ln \varphi^q(r) - \ln \varphi^{q+1}(r)] \quad (7)
$$

which can be estimated by the statistic,

$$FuzzEn(q, r, N) = \ln \varphi^q(r) - \ln \varphi^{q+1}(r) \qquad (8)$$

where r and q indicate the width of the boundary for similarity measurement and the length of the compared window, respectively. N denotes the length of the TVSFC time series. Herein, following the previous study, q was determined to be 2, and r was defined as 0.2 times the standard deviation of the SFC time series[11].

The estimation of SFC temporal variability $\in \mathbb{R}^{308 \times 1}$ for each participant allows us to derive the spatial distribution of SFC temporal variability by averaging the variability vectors across all participants. Subsequently, the 10% to 50% cortical regions representing the largest and smallest fuzzy entropy were extracted to index the complementary spatial architectures of SFC variability. In addition, the regional structural connectivity was generated by calculating the degree of MSN, which was further Z-scored. The functional network was constructed using Pearson's correlation of pairwise fMRI signals, and the corresponding degree was calculated and Z-scored to exhibit the regional functional connectivity. Meanwhile, the traditional static SFC was computed by correlating the morphometric similarity and functional connectivity profiles of each region, followed by Z-scoring. Thereafter, spatial correlations between SFC temporal variability and regional structural connectivity, functional connectivity, as well as static SFC were investigated. A "spin"-based permutation test (5000 times) was adopted to correct the spatial autocorrelation[26].

Partial least squares analysis between SFC variability and behavior measures

Herein, PLS analysis was employed to investigate the multivariate relationships between cortical SFC variability and 59 available behavior measures (Table 1). As an unsupervised machine-learning technique, PLS analysis identifies latent components by discerning weighted patterns of two multivariables that exhibit maximum covariance with each other[62]. The permutation test was employed to determine the number of significant latent components (5000 permutations). Each latent component is characterized by a unique profile of behavior (referred to as behavioral saliences) and SFC variability distribution (referred to as SFC variability saliences). By linearly projecting the SFC variability and behavioral measures of each participant onto their respective saliences, we obtain individual-specific SFC variability and behavioral composite scores for each latent component. Pearson's correlation between SFC variability (behavioral) composite scores and the original SFC variability data (behavioral measures) was calculated to interpret the corresponding latent component. A strong positive (or negative) association with respect to a specific behavioral trait (SFC variability measure) suggests the heightened significance of the behavioral trait (SFC variability measure) for the corresponding latent component. Then, the confidence intervals for these correlations were determined by a bootstrapping procedure[63] that generated 1000 samples with replacement from the original behavioral and SFC variability data. The correlation coefficients were divided by their estimated standard deviation obtained through bootstrap to calculate the Z-scores, which were further transformed into p-values and subjected to either FDR correction or Bonferroni correction. Notably, prior to the PLS analysis, confounding effects, including age and sex, were regressed out from both behavioral and SFC variability data.

Additionally, a reliability analysis was performed by incorporating confounding variables (age and sex) into the behavioral data for the PLS analysis[28]. To evaluate the robustness of each latent component, Pearson's correlation was calculated between the SFC variability (or behavioral) salience derived from the reliability analysis and that obtained from the original PLS analysis.

Transcription-neuroimaging association analysis

Brain-wide gene expressions are extracted from the AHBA transcriptomic dataset (http://human.brain-map.org; Supplementary Table S11)[13] using a standard pre-processing protocol (https://github.com/BMHLab/AHBAprocessing; See the Supplementary Methods 1 for further details)[16]. Given the limited data available for the right hemisphere in the AHBA dataset, our subsequent analysis was focused only on the left hemisphere of the D-K atlas, i.e., 152 regions × 10,027 gene expression levels[64]. Then, PLS regression was employed to probe the potential relationship between cortical SFC variability and transcriptional levels for all genes. Thereinto, gene expression levels were regarded as predictor variables to predict the regional SFC variability in 152 brain regions located in the left hemisphere. PLS1 depicted the most correlated cortical expression map with respect to the temporal variability in cortical SFC. Additionally, a "spin"-based permutation test (5000 times) was adopted to correct the spatial autocorrelation[26]. The bootstrapping technique was performed to evaluate the contribution of each gene to the PLS1. The Z-score per gene was determined by dividing its weight by the corresponding bootstrap standard error, based on which all 10,027 genes were ranked. Then, genes exhibiting Z > 3 and FDR < 0.05 were assigned to the PLS1+ gene list, while those with Z < -3 and FDR < 0.05 were allocated to the PLS1- gene list.

Enrichment analyses

Subsequently, the PLS1+ and PLS1− gene lists were separately subjected to the Metascape analysis[65] to identify enriched KEGG pathways and GO biological processes. The enrichment pathways that survived after FDR correction ($p_{FDR} < 0.01$) were retained. For cell-type specific expression analysis, we first obtained gene profiles of 7 cell types from 5 single-cell research[66]. To assign SFC variability-related genes obtained by PLS analysis to cell types, we overlapped the gene set of each cell type with the PLS1+ (or PLS1−) gene list. Subsequently, we resampled the genes involved in cell types 5000 times to test the null hypothesis that the PLS1+ (or PLS1−) gene list was randomly assigned to different cell types[64]. The p_{perm} was obtained by the occupied null models (<5th, or >95th centile) and corrected by FDR. With the identical strategy, we performed cortical layer enrichment utilizing marker genes identified from a prior transcriptomic investigation[30].

Genes enriched for brain diseases

Based on several publicly curated disease gene databases, including DisGeNET, OMIM, and GLAD4U databases, the WebGestalt tool (http://www.webgestalt.org/)[31] was adopted to explore the enrichment of brain disease for cortical SFC variability-specific genes. The top ten terms were summarized by the ranked p-value.

Neurotransmitter receptors and transporters analysis

We further test whether brain SFC variability was spatially correlated with the distribution of 9 distinct neurotransmitter systems derived from previously reported PET images (https://github.com/netneurolab/hansen_receptors)[19]. The detailed information for receptors and transporters can be found in Supplementary Table S4. PET images of each neurotransmitter receptor/transporter were averaged across participants and then standardized using Z-scores. The spatial correlation between SFC variability distribution and each neurotransmitter receptor/ transporter was performed. To account for the spatial autocorrelation of brain regions, a "spin"-based spatial permutation test[26] was conducted 5000 times, followed by FDR correction.

Subsequently, we fit a multiple linear regression model that predicts the cortical SFC variability from related neurotransmitter receptor and transporter densities. However, due to inherent spatial autocorrelation, proximal regions exhibit similar neurotransmitter profiles and SFC variability[67]. To minimize the dependence between

the two data sets caused by spatial autocorrelation, out-of-sample cross-validation with a distance-dependent method[32] was conducted to assess predictive generalization. Specifically, for each of the 308 brain regions (from the D-K atlas), we defined a training set comprising the 75% nearest regions (in Euclidean space), and used it to train the regression model. The model was then used to predict SFC variability in the remaining 25% of regions, and the predicted test set output variable (regional SFC variability) was correlated to the actual test set values. This procedure was repeated 308 times, yielding a distribution of cross-validated correlations that reflects the model's ability to generalize to spatially distinct areas.

Additionally, the relative contribution of a specific neurotransmitter system to the overall fit (adjusted R^2) in the multiple linear regression model was evaluated by dominance analysis[33] (See Supplementary Methods 2 for further details).

Robustness and sensitivity analyses

The above cortical SFC variability was further validated in an independent replication cohort, i.e., the CHCP cohort. Firstly, the SFC temporal variability distribution of the CHCP cohort was calculated following the same procedures as the HCP cohort. Spatial correlation between HCP and CHCP cohorts was further performed to examine the replicability of brain SFC temporal variability. Then, we utilized PLS regression to map the variations in SFC variability of the CHCP cohort to brain-wide gene expression of the AHBA. A multi-gene list meta-analysis[29] was performed between the PLS1+ (PLS1−) genes of the two cohorts. The enrichment pathways that survived after FDR correction ($p_{FDR} < 0.01$) were retained.

Based on two different strategies, the validity of our proposed SFC variability analysis was accordingly demonstrated. First, in addition to MSN, WMN and MPCN were also constructed to measure inter-regional structural relationships. Following the same strategy, WMN-derived and MPCN-derived SFC variability was subsequently established, and their relationships with individual behavioral measures and brain-wide gene expression were further explored. Second, to evaluate the influence of edge-level spatial proximity on SFC variability, following previous studies[35,36], we calculated tvSFC by utilizing the partial correlation between morphometric similarity and functional co-fluctuation connectivity while regressing the shared relationship with anatomical distance. After recomputing the SFC temporal variability, the spatial correlation between SFC temporal variability maps with and without the regression of Euclidean distance was calculated. A "*spin*"-based permutation test (5000 times) was adopted to correct the spatial autocorrelation on the ROI level[26].

Reporting summary

Further information on research design is available in the Nature Portfolio Reporting Summary linked to this article.

Data availability

The MRI data of the HCP and CHCP cohorts are publicly available at https://db.humanconnectome.org/ and https://cstr.cn/31253.11.sciencedb.01374, respectively. The transcriptomic dataset of 6 post-mortem adult brains can be found in the Allen Brain Atlas ("Complete normalized microarray datasets", https://human.brain-map.org/static/download). Compiled cell-specific genes are available at https://static-content.springer.com/esm/art%3A10.1038%2Fs41467-020-17051-5/MediaObjects/41467_2020_17051_MOESM8_ESM.xlsx. Disease-association terms are available at the WebGestalt website (http://www.webgestalt.org/). Different layer markers are available at https://static-content.springer.com/esm/art%3A10.1038%2Fnn.4548/MediaObjects/41593_2017_BFnn4548_MOESM255_ESM.xlsx. Neurotransmitter maps are publicly available at https://github.com/netneurolab/hansen_receptors. Source data are provided with this paper.

Code availability

The MRI preprocessing software is freely available (FreeSurfer v6.0, http://surfer.nmr.mgh.harvard.edu/, DPABI v7.0, https://rfmri.org/DPABI, and FSL v6.0, https://fsl.fmrib.ox.ac.uk/fsl/fslwiki). The temporal variability and statistical analyses were conducted using MATLAB R2018b (https://ww2.mathworks.cn/products/matlab.html). The code for behavioral PLS analysis is available at https://github.com/danizoeller/myPLS. The standard protocol for gene expression analysis is available at https://github.com/BMHLab/AHBAprocessing. The code for PLS analysis of gene expression profiles is available at https://github.com/SarahMorgan/Morphometric_Similarity_SZ. The code for *spin*-based permutation testing of cortical correlations is available at https://github.com/frantisekvasa/rotate_parcellation. Metascape analyses were performed at https://metascape.org/gp/index.html#/main/step1. The code for neurotransmitter receptor and transporter analysis by multiple linear regression model is available at https://github.com/netneurolab/hansen_receptors. The dominance analysis is available at https://github.com/dominance-analysis/dominance-analysis.

References

1. Park, H.-J. & Friston, K. Structural and functional brain networks: from connections to cognition. *Science* **342**, 1238411 (2013).
2. Seguin, C., Sporns, O. & Zalesky, A. Brain network communication: concepts, models and applications. *Nat. Rev. Neurosci.* **24**, 557–574 (2023).
3. Fotiadis, P. et al. Structure–function coupling in macroscale human brain networks. *Nat. Rev. Neurosci.* **25**, 688–704 (2024).
4. Baum, G. L. et al. Development of structure–function coupling in human brain networks during youth. *Proc. Natl Acad. Sci. USA* **117**, 771–778 (2020).
5. Gu, Z., Jamison, K. W., Sabuncu, M. R. & Kuceyeski, A. Heritability and interindividual variability of regional structure-function coupling. *Nat. Commun.* **12**, 4894 (2021).
6. Zhang, X. et al. Structural and functional deficits and couplings in the cortico-striato-thalamo-cerebellar circuitry in social anxiety disorder. *Transl. Psychiatr.* **12**, 26 (2022).
7. Liu, Z.-Q. et al. Time-resolved structure-function coupling in brain networks. *Commun. Biol.* **5**, 532 (2022).
8. Fukushima, M. & Sporns, O. Structural determinants of dynamic fluctuations between segregation and integration on the human connectome. *Commun. Biol.* **3**, 606 (2020).
9. Faskowitz, J., Esfahlani, F. Z., Jo, Y., Sporns, O. & Betzel, R. F. Edge-centric functional network representations of human cerebral cortex reveal overlapping system-level architecture. *Nat. Neurosci.* **23**, 1644–1654 (2020).
10. Seidlitz, J. et al. Morphometric similarity networks detect micro-scale cortical organization and predict inter-individual cognitive variation. *Neuron* **97**, 231–247.e237 (2018).
11. Li, F. et al. Brain variability in dynamic resting-state networks identified by fuzzy entropy: a scalp EEG study. *J. Neural Eng.* **18**, 046097 (2021).
12. Chen, W., Zhuang, J., Yu, W. & Wang, Z. Measuring complexity using fuzzyen, apen, and sampen. *Med. Eng. Phys.* **31**, 61–68 (2009).
13. Hawrylycz, M. J. et al. An anatomically comprehensive atlas of the adult human brain transcriptome. *Nature* **489**, 391–399 (2012).
14. Cassidy, P. J. & Radda, G. K. Molecular imaging perspectives. *J. R. Soc. Interface* **2**, 133–144 (2005).
15. Martins, D. et al. Imaging transcriptomics: convergent cellular, transcriptomic, and molecular neuroimaging signatures in the healthy adult human brain. *Cell Rep.* **37**, 110173 (2021).
16. Arnatkevičiūtė, A., Fulcher, B. D. & Fornito, A. A practical guide to linking brain-wide gene expression and neuroimaging data. *Neuroimage* **189**, 353–367 (2019).
17. Markello, R. D. et al. Standardizing workflows in imaging transcriptomics with the abagen toolbox. *eLife* **10**, e72129 (2021).

18. Arnatkeviciute, A., Markello, R. D., Fulcher, B. D., Misic, B. & Fornito, A. Toward best practices for imaging transcriptomics of the human brain. *Biol. Psychiatry* **93**, 391–404 (2023).

19. Hansen, J. Y. et al. Mapping neurotransmitter systems to the structural and functional organization of the human neocortex. *Nat. Neurosci.* **25**, 1569–1581 (2022).

20. Hänisch, B. et al. Cerebral chemoarchitecture shares organizational traits with brain structure and function. *eLife* **12**, e83843 (2023).

21. Van Essen, D. C. et al. The Human Connectome Project: a data acquisition perspective. *Neuroimage* **62**, 2222–2231 (2012).

22. Ge, J. et al. Increasing diversity in connectomics with the Chinese Human Connectome Project. *Nat. Neurosci.* **26**, 163–172 (2023).

23. Morgan, S. E. et al. Cortical patterning of abnormal morphometric similarity in psychosis is associated with brain expression of schizophrenia-related genes. *Proc. Natl Acad. Sci. USA* **116**, 9604–9609 (2019).

24. Yeo, B. T. T. et al. The organization of the human cerebral cortex estimated by intrinsic functional connectivity. *J. Neurophysiol.* **3**, 1125–1165 (2011).

25. von Economo, C. F., Koskinas, G. N. & Triarhou, L. C. Atlas of cytoarchitectonics of the adult human cerebral cortex. (S Karger AG, 2008).

26. Váša, F. et al. Adolescent tuning of association cortex in human structural brain networks. *Cereb. Cortex* **28**, 281–294 (2018).

27. Straathof, M., Sinke, M. R. T., Dijkhuizen, R. M. & Otte, W. M. A systematic review on the quantitative relationship between structural and functional network connectivity strength in mammalian brains. *J. Cereb. Blood Flow. Metab.* **39**, 189–209 (2019).

28. Wang, Y. et al. Covariance patterns between sleep health domains and distributed intrinsic functional connectivity. *Nat. Commun.* **14**, 7133 (2023).

29. Zhou, Y. et al. Metascape provides a biologist-oriented resource for the analysis of systems-level datasets. *Nat. Commun.* **10**, 1523 (2019).

30. He, Z. et al. Comprehensive transcriptome analysis of neocortical layers in humans, chimpanzees and macaques. *Nat. Neurosci.* **20**, 886–895 (2017).

31. Wang, J., Vasaikar, S., Shi, Z., Greer, M. & Zhang, B. WebGestalt 2017: a more comprehensive, powerful, flexible and interactive gene set enrichment analysis toolkit. *Nucleic Acids Res* **45**, W130–W137 (2017).

32. Hansen, J. Y. et al. Mapping gene transcription and neurocognition across the human neocortex. *Nat. Hum. Behav.* **5**, 1240–1250 (2021).

33. Azen, R. & Budescu, D. V. The dominance analysis approach for comparing predictors in multiple regression. *Psychol. Methods* **8**, 129 (2003).

34. Paquola, C. et al. Microstructural and functional gradients are increasingly dissociated in transmodal cortices. *PLoS. Biol.* **17**, e3000284 (2019).

35. Honey, C. J. et al. Predicting human resting-state functional connectivity from structural connectivity. *Proc. Natl Acad. Sci. USA* **106**, 2035–2040 (2009).

36. Horn, A., Ostwald, D., Reisert, M. & Blankenburg, F. The structural–functional connectome and the default mode network of the human brain. *Neuroimage* **102**, 142–151 (2014).

37. Monroe, J. F. et al. The fusiform response to faces: explicit versus implicit processing of emotion. *Hum. Brain Mapp.* **34**, 1–11 (2013).

38. Seeley, W. W. The salience network: a neural system for perceiving and responding to homeostatic demands. *J. Neurosci.* **39**, 9878–9882 (2019).

39. Lima Portugal, L. C. et al. Interactions between emotion and action in the brain. *Neuroimage* **214**, 116728 (2020).

40. Vimal, R. L. P. Attention and emotion. *Annu. Rev. Biomed. Data Sci.* **10**, 84–104 (2008).

41. Ochsner, K. N., Silvers, J. A. & Buhle, J. T. Functional imaging studies of emotion regulation: a synthetic review and evolving model of the cognitive control of emotion. *Ann. N. Y. Acad. Sci.* **1251**, E1–E24 (2012).

42. Burns, M. E. & Augustine, G. J. Synaptic structure and function: dynamic organization yields architectural precision. *Cell* **83**, 187–194 (1995).

43. Dehay, C. & Kennedy, H. Cell-cycle control and cortical development. *Nat. Rev. Neurosci.* **8**, 438–450 (2007).

44. Sanacora, G., Treccani, G. & Popoli, M. Towards a glutamate hypothesis of depression: an emerging frontier of neuropsychopharmacology for mood disorders. *Neuropharmacology* **62**, 63–77 (2012).

45. Yan, Z. & Rein, B. Mechanisms of synaptic transmission dysregulation in the prefrontal cortex: pathophysiological implications. *Mol. Psychiatr.* **27**, 445–465 (2022).

46. Pfanner, N., Warscheid, B. & Wiedemann, N. Mitochondrial proteins: from biogenesis to functional networks. *Nat. Rev. Mol. Cell Biol.* **20**, 267–284 (2019).

47. Pei, L. & Wallace, D. C. Mitochondrial etiology of neuropsychiatric disorders. *Biol. Psychiatry* **83**, 722–730 (2018).

48. Lee, Y. M. et al. Mitochondrial respiratory chain defects: underlying etiology in various epileptic conditions. *Epilepsia* **49**, 685–690 (2008).

49. Kim, S. & Sabatini, B. L. Analytical approaches to examine gamma-aminobutyric acid and glutamate vesicular co-packaging. *Front. Synaptic Neurosci.* **14**, 1076616 (2023).

50. Tritsch, N. X., Granger, A. J. & Sabatini, B. L. Mechanisms and functions of GABA co-release. *Nat. Rev. Neurosci.* **17**, 139–145 (2016).

51. Shine, J. M. Neuromodulatory influences on integration and segregation in the brain. *Trends Cogn. Sci.* **23**, 572–583 (2019).

52. Donahue, C. J. et al. Using diffusion tractography to predict cortical connection strength and distance: a quantitative comparison with tracers in the monkey. *J. Neurosci.* **36**, 6758–6770 (2016).

53. Maier-Hein, K. H. et al. The challenge of mapping the human connectome based on diffusion tractography. *Nat. Commun.* **8**, 1349 (2017).

54. Sebenius, I. et al. Structural MRI of brain similarity networks. *Nat. Rev. Neurosci.* **26**, 42–59 (2025).

55. Calhoun, V. D., Miller, R., Pearlson, G. & Adalı, T. The chronnectome: time-varying connectivity networks as the next frontier in fMRI data discovery. *Neuron* **84**, 262–274 (2014).

56. Fulcher, B. D., Arnatkeviciute, A. & Fornito, A. Overcoming false-positive gene-category enrichment in the analysis of spatially resolved transcriptomic brain atlas data. *Nat. Commun.* **12**, 2669 (2021).

57. Wang, Y. et al. Uncovering the genetic profiles underlying the intrinsic organization of the human cerebellum. *Mol. Psychiatr.* **27**, 2619–2634 (2022).

58. Wu-Minn, H. C. P. 1200 subjects data release reference manual. https://www.humanconnectome.org (2017).

59. Dale, A. M., Fischl, B. & Sereno, M. I. Cortical Surface-based analysis: I. Segmentation and surface reconstruction. *Neuroimage* **9**, 179–194 (1999).

60. Fischl, B. et al. Automatically parcellating the human cerebral cortex. *Cereb. Cortex* **14**, 11–22 (2004).

61. Jenkinson, M., Beckmann, C. F., Behrens, T. E., Woolrich, M. W. & Smith, S. M. Fsl. *Neuroimage* **62**, 782–790 (2012).

62. Dong, D. et al. Linking cerebellar functional gradients to transdiagnostic behavioral dimensions of psychopathology. *NeuroImage-Clin.* **36**, 103176 (2022).

63. Efron, B. & Tibshirani, R. Bootstrap methods for standard errors, confidence intervals, and other measures of statistical accuracy. *Stat. Sci.* **1**, 54–75 (1986).

64. Li, J. et al. Cortical structural differences in major depressive disorder correlate with cell type-specific transcriptional signatures. *Nat. Commun.* **12**, 1–14 (2021).
65. Zhou, Y. et al. Metascape provides a biologist-oriented resource for the analysis of systems-level datasets. *Nat. Commun.* **10**, 1–10 (2019).
66. Seidlitz, J. et al. Transcriptomic and cellular decoding of regional brain vulnerability to neurogenetic disorders. *Nat. Commun.* **11**, 1–14 (2020).
67. Burt, J. B., Helmer, M., Shinn, M., Anticevic, A. & Murray, J. D. Generative modeling of brain maps with spatial autocorrelation. *Neuroimage* **220**, 117038 (2020).

Author contributions
Conceptualization: P.X. and J.L. Supervision: P.X., F.L., and D.D. Data resources: D.D., S.G., and S.E. Methodology: L.J. and J.Y. Analysis: L.J., Y.Z., and G.W. Visualization: R.H. and J.Y. Writing—original draft: L.J., F.L., and P.X. Writing—review and editing: S.E., D.Y., S.G., F.W., and P.V. Funding acquisition: P.X., F.L., and D.Y.

Competing interests
The authors declare that they have no competing interests.

Additional information
Supplementary information The online version contains supplementary material available at https://doi.org/10.1038/s41467-025-63000-5.

Correspondence and requests for materials should be addressed to Dezhong Yao, Debo Dong, Fali Li or Peng Xu.

Peer review information *Nature Communications* thanks the anonymous reviewer(s) for their contribution to the peer review of this work. A peer review file is available.

Reprints and permissions information is available at http://www.nature.com/reprints

Publisher's note Springer Nature remains neutral with regard to jurisdictional claims in published maps and institutional affiliations.